

# The Matrix Element Method at Next-to-Leading Order.

---

**John M. Campbell, Walter T. Giele and Ciaran Williams**

*Fermilab, Batavia, IL 60510, USA*

*E-mails: johnmc@fnal.gov, giele@fnal.gov, ciaran@fnal.gov.*

**ABSTRACT:** This paper presents an extension of the matrix element method to next-to-leading order in perturbation theory. To accomplish this we have developed a method to calculate next-to-leading order weights on an event-by-event basis. This allows for the definition of next-to-leading order likelihoods in exactly the same fashion as at leading order, thus extending the matrix element method to next-to-leading order. A welcome by-product of the method is the straightforward and efficient generation of unweighted next-to-leading order events. As examples of the application of our next-to-leading order matrix element method we consider the measurement of the mass of the  $Z$  boson and also the search for the Higgs boson in the four lepton channel.

**KEYWORDS:** Hadron colliders, NLO Computations, Higgs Physics.

---

## Contents

<b>1. Introduction</b>	<b>1</b>
<b>2. The Matrix Element Method at Leading Order</b>	<b>3</b>
2.1 Overview of the MEM	3
2.2 Leading order formulation	4
<b>3. The Matrix Element Method at Next-to-Leading Order</b>	<b>8</b>
3.1 Going beyond LO: Defining NLO on an event by event basis	8
3.2 Generating unweighted events at NLO	11
<b>4. Validation</b>	<b>12</b>
4.1 Physics in the MEM frame.	12
4.2 Validating the MEM: measuring $m_Z$	15
<b>5. The Higgs Boson search in the channel <math>H \rightarrow ZZ \rightarrow 4\ell</math></b>	<b>17</b>
5.1 Event selection	18
5.2 Higgs mass limits in the absence of the signal process	18
5.3 Results in the presence of a Higgs boson with $m_H = 125$ GeV	20
5.4 Results in the presence of a Higgs boson with $m_H = 425$ GeV	22
5.5 A study with multiple pseudo experiments	22
<b>6. Conclusions</b>	<b>24</b>
<b>A. An Initial State Forward Branching Phase Space Generator</b>	<b>26</b>
<b>B. Subtraction terms in the MEM frame</b>	<b>28</b>

---

## 1. Introduction

The continued successful running of the LHC is already resulting in an impressive data set with which to test the Standard Model (SM). One of the main aims of the experimental program is to observe the mechanism behind electroweak symmetry breaking, for which the postulated Higgs boson is a theoretically well-motivated example. Using the  $5\text{ fb}^{-1}$  data set the LHC has tightly constrained the mass of the Higgs boson, whilst also providing tantalising hints in the low mass region ( $\sim 120 - 125$  GeV) [1, 2]. Present analyses often use data driven techniques for background estimation with an emphasis on accurate signal modeling, for instance in the diphoton Higgs search [3, 4]. Whilst this is a sensible strategy for searches, after discovery an accurate modeling of both signal and background will be

required in order to confirm the exact properties of any new particle, such as its spin and couplings [5, 6]. In addition to Higgs searches, precision measurements in the electroweak sector of the SM could also provide valuable insight. By measuring top quark properties and electroweak gauge boson couplings, potential new physics contributions can be constrained. A recent example, that exhibits some tension with the SM, is provided by measurements of the top quark forward-backward asymmetry at the Tevatron [7, 8].

There are many methods available for performing studies of particle properties, for instance for measuring their masses or investigating their interactions. Among these, the matrix element method (MEM) stands out since it is sensitive to all the available kinematic information for each individual event. Originally pioneered at the Tevatron [9, 10], the MEM has proven extremely useful in the top sector [11–16]. Recently the method has been used to observe single top production [17–20] and to provide evidence for top quark spin correlations [21]. The MEM has also been used to try to improve searches for the Higgs boson in the associated production channel [22]. At the LHC the MEM is also beginning to be used, for example in the measurement of the electroweak mixing angle at CMS [23].

The popularity of the MEM is based on its ability to utilize the theoretical prediction from the matrix element, retaining all the hard scattering correlations. For each experimental event, the MEM assigns a probability that it can be described by a given theoretical model. In this way one can produce a likelihood that the theoretical model describes a particular set of data. Matrix elements (at tree-level) are relatively straightforward to calculate and automated tools for this purpose have been available for several years [24–28]. Indeed, the application of automated tools to the MEM was previously considered in ref. [29]. However, a serious limitation of the method is that it has so far been defined only at leading order (LO). For the precision studies that will become possible with the wealth of data at the LHC, it is crucial to extend and adapt the method such that it is defined at higher orders. An implementation of the method at next-to-leading order (NLO), the de facto standard for most theoretical predictions at the LHC, is required to put the MEM on a solid theoretical footing and elevate the method to being a robust analysis tool.

The absence of higher order corrections in current implementations of the MEM is easily understood. It is not immediately clear how to use existing NLO calculations to associate a NLO weight with a given exclusive experimental event. This is primarily due to the fact that NLO calculations include contributions from both loop and bremsstrahlung diagrams, that must be integrated over different physical phase spaces. As such there is no clear one-to-one map between an exclusive event, containing a finite number of objects with measured properties, and a NLO weight. Addressing this very issue is the principal goal of this paper.

We therefore present a method of calculating NLO weights suitable for use with the MEM approach. As a welcome by-product, the method also provides a procedure for calculating unweighted NLO events. As a first step, in this paper we consider only the production of colour neutral final states. This ensures that at NLO the real phase space is associated with radiation from initial state partons only. We thus postpone the treatment of final state jets at NLO to a future publication.

This paper proceeds as follows. In section 2 we first introduce the MEM at LO and discuss its use in experimental analyses. Section 3 explains our extension of the MEM to NLO and discusses the generation of unweighted NLO events. In section 4 we validate the code using MCFM [30–33] and Pythia [34]. Section 5 is devoted to an application of immediate phenomenological interest, namely the search for a Higgs boson in the  $ZZ^*$  decay channel to four leptons. Finally in section 6 we draw our conclusions. The appendices describe the generation of the phase space in more detail and discuss the modifications to the usual dipole subtraction procedure that are required in our approach.

## 2. The Matrix Element Method at Leading Order

In this section we define the MEM at LO and discuss how it may be used in experimental analyses.

### 2.1 Overview of the MEM

We begin by assuming that one wishes to measure a model parameter  $\Omega$ , using an experimental data set  $\{\mathbf{x}\}$  that contains  $N$  events  $\mathbf{x}_i$ . One method to determine the best-fit value of  $\Omega$  is to construct a probability density function in which each event is weighted by the LO scattering probability computed with the parameter  $\Omega$ . The resulting probability density function associated with a single event  $\mathbf{x}$ , for a given  $\Omega$ , can be written schematically as,

$$\mathcal{P}(\mathbf{x}|\Omega) = \frac{1}{\sigma_{\Omega}^{LO}} \int dx_a dx_b d\mathbf{y} \sum_{ij} \frac{f_i(x_a) f_j(x_b)}{x_a x_b s} \mathcal{B}_{\Omega}^{ij}(p_a, p_b, \mathbf{y}) W(\mathbf{x}, \mathbf{y}) . \quad (2.1)$$

In this equation  $f_i(x_a)$  and  $f_j(x_b)$  represent the parton distribution functions for partons of flavours  $i$  and  $j$  possessing momentum fractions  $x_a$  and  $x_b$  of their parent hadrons.  $\mathcal{B}_{\Omega}^{ij}(p_a, p_b, \mathbf{y})$  is the LO scattering probability with partons  $i$  and  $j$  in the initial state. The hadron collision takes place at a centre of mass energy  $\sqrt{s}$  while the flux factor entering in the denominator of Eq. (2.1) is the partonic centre of mass energy squared,  $s_{ab} = x_a x_b s$ .

An experimental event  $\mathbf{x}$  is by definition a detector level event, whilst the scattering probability is computed theoretically at the level of partons. Therefore in order to correctly use the scattering probability as a probability density function one must include effects that model this discrepancy. The transfer function  $W(\mathbf{x}, \mathbf{y})$  relates a detector level event  $\mathbf{x}$  to a particle level event  $\mathbf{y}$  that can be used to compute the scattering amplitude. This transfer function, dependent on the specifics of the experimental set-up, takes account of factors such as limitations on the energy resolution and acceptance of the detector. The transfer function is constructed such that it is itself a probability density function,

$$\int d\mathbf{y} W(\mathbf{x}, \mathbf{y}) = 1 . \quad (2.2)$$

Finally, the factor  $\sigma_{\Omega}$  is the total cross section for the process for a specific choice of  $\Omega$ , thus ensuring that the probability distribution is properly normalized to unity.

Once the probability density function  $\mathcal{P}(\mathbf{x}|\Omega)$  has been computed for each event  $\mathbf{x}$ , it is straightforward to compute a likelihood for the data set as a whole. For the data set  $\{\mathbf{x}\}$  with  $N$  events, the likelihood function  $\mathcal{L}(\{\mathbf{x}\}|\Omega)$  for a given parameter  $\Omega$  is defined by,

$$\mathcal{L}(\{\mathbf{x}\}|\Omega) = f(N) \prod_{i=1}^N \mathcal{P}(\mathbf{x}_i|\Omega). \quad (2.3)$$

Here  $f(N)$  is a normalisation factor related to the overall number of events in the data set. In most analyses one is interested in comparing two hypotheses, either in the form of a likelihood ratio, or more commonly by comparing the difference of two log-likelihoods. Therefore in most practical applications the explicit form of  $f(N)$  is unimportant. This is the case for all the examples that we present here and, as such, we will simply drop the factor  $f(N)$  in Eq. (2.3).

By construction, the value of the likelihood function will be larger for theories that describe the data better. The best fit corresponds to the parameter choice  $\Omega$  that maximises  $\mathcal{L}$  (and hence also  $\log \mathcal{L}$ ). In the region of the maximum – and as long as the data set is large enough – departures from the maximum value of the likelihood can be simply interpreted in terms of standard deviations from the best fit. Since we consider a single parameter  $\Omega$ , the likelihood can be described by a parabola in the region of the maximum (see e.g. ref [35]) and standard deviations (here represented by  $n\sigma$ ) from the observed maximum can then be defined by,

$$\log \mathcal{L} |_{n\sigma} = \log \mathcal{L}_{max} - n^2/2. \quad (2.4)$$

In our examples we will use this to define one- and two-sigma confidence levels for our results, although we stress that our studies do not include detector effects and are thus only for the sake of illustration.

## 2.2 Leading order formulation

We now return to the probability density function, Eq. (2.1). We recall that at this order,

$$\mathcal{B}_{\Omega}^{ij}(p_a, p_b, \mathbf{y}) = |\mathcal{M}_{\Omega}^{ij,(0)}(p_a, p_b, \mathbf{y})|^2, \quad (2.5)$$

where  $\mathcal{M}_{\Omega}^{ij,(0)}(\mathbf{y})$  is the leading order matrix element for the relevant process with initial state partons  $i$  and  $j$ . In this paper we make the simplifying assumption that the events completely specify the final state particles so that, for example, we do not consider events containing neutrinos. For a Born point  $p$  the constraint of momentum conservation fixes the values of the parton fractions  $x_a$  and  $x_b$ . By convention we position the incoming particles along the  $z$ -axis in the lab frame and then use the momentum conserving delta function between the  $n$  final-state particles  $\{p_1, \dots, p_n\}$ ,

$$\delta^{(4)}(p_a + p_b - \sum_{i=1}^n p_i), \quad (2.6)$$

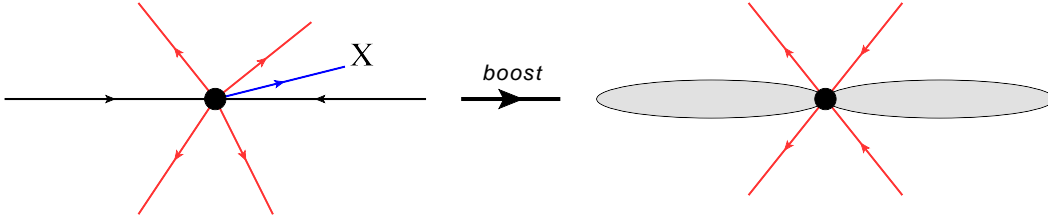


**Figure 1:** The generation of the Born (and virtual) phase space from a given experimental event. The left hand side depicts a collision that results in the production of a colour neutral final state (represented here by four leptons in red) that do not balance in the transverse plane. The resulting imbalance ( $X$ , in blue) represents the remaining event which is not modelled in the Born matrix element. We apply a Lorentz transformation such that  $X$  has no components in the transverse plane, with the remaining longitudinal and energy components absorbed into the colliding partons.

to find the relations,

$$x_a - x_b = \frac{2}{\sqrt{s}} \left( \sum_{i=1}^n p_i^z \right), \quad x_a + x_b = \frac{2}{\sqrt{s}} \left( \sum_{i=1}^n E_i \right). \quad (2.7)$$

However, matching an experimental point  $\tilde{p}$  to the LO kinematics ( $p$ ) is a challenge. In particular, any event will always contain additional radiation that is not modelled by the leading order (Born level) matrix element. In order to proceed we shall define a four vector  $X$ , that balances the momenta of the final state particles. This is illustrated schematically in Fig. 1 and expressed through the equations,

$$X = - \sum_{i=1}^n \tilde{p}_i. \quad (2.8)$$

The Born matrix elements, with the beam directions consistently along the  $z$ -axis, are only defined for  $X^x = X^y = 0$ , i.e. when there is no  $p_T$  imbalance between the final state particles<sup>1</sup>. Therefore, in order to ensure that the experimental event has a well-defined interpretation as a Born level phase space point we need to remove the transverse components of  $X$ . This can be achieved by applying a Lorentz transformation  $\Lambda(X)$  on the momenta  $\tilde{p}$  in the event to arrive at a frame in which the transverse components of  $X$  are zero,

$$p_i^\mu = \Lambda^\mu_\nu(X) \tilde{p}_i^\nu \quad \text{with} \quad \sum_{i=1}^n p_i^x = \sum_{i=1}^n p_i^y = 0. \quad (2.9)$$

As desired, the phase space point  $p$  is now of the correct form to be used in a Born level matrix element. For a given transformation, the momentum fractions  $x_a$  and  $x_b$  are then related to the transformed momenta  $p$  through the relations in Eq. (2.7). However, we note

---

<sup>1</sup>Attempting to evaluate a LO matrix element with a phase space point that does not conserve momentum is ill-defined. The exact weight obtained depends on which kinematic invariants one has chosen to use in the expression for the matrix element.

that Eq. (2.9) does not specify a unique transformation. We can define multiple transformations that result in  $X^x = X^y = 0$  and that yield different longitudinal components of  $p$ . In other words  $x_a$  and  $x_b$  are frame-dependent quantities determined by the boost choice and it is only the product  $x_a x_b$  that is Lorentz invariant. Therefore in order to produce a sensibly defined weight for each event we must integrate over this unobservable degree of freedom.

To illustrate these ideas in more detail we begin with the usual definition of the total cross section for the production of  $n$  massless final state particles,

$$\sigma_\Omega^{LO} = (2\pi)^{4-3n} \int dx_a dx_b \prod_{m=1}^n \left( \frac{d^3 \mathbf{p}_m}{2E_m} \right) \frac{f_i(x_a) f_j(x_b)}{x_a x_b s} \mathcal{B}_\Omega^{ij} \delta^{(4)} \left( p_a + p_b - \sum_{i=1}^n p_i \right). \quad (2.10)$$

Here we have suppressed the dependence of  $\mathcal{B}$  on the kinematics and the summation over  $i$  and  $j$  for clarity. We wish to factorise Eq. (2.10) into two pieces, one representing initial state production and the other the decay of a heavy object into the final state particles. To this end we define  $Q = p_a + p_b$  and insert the operator  $\int dQ^2 \delta(x_a x_b s - Q^2) = 1$ ,

$$\begin{aligned} \sigma_\Omega^{LO} &= (2\pi)^{4-3n} \int dx_a dx_b dQ^2 \delta(x_a x_b s - Q^2) \\ &\times \prod_{m=1}^n \left( \frac{d^3 \mathbf{p}_m}{2E_m} \right) \frac{f_i(x_a) f_j(x_b)}{x_a x_b s} \mathcal{B}_\Omega^{ij} \delta^{(4)} \left( Q - \sum_{m=1}^n p_m \right). \end{aligned} \quad (2.11)$$

For the remainder of this paper we will define the phase space element associated with the final state particles as,

$$d\mathbf{x} = (2\pi)^{4-3n} dQ^2 \prod_{m=1}^n \left( \frac{d^3 \mathbf{p}_m}{2E_m} \right) \delta^{(4)} \left( Q - \sum_{m=1}^n p_m \right). \quad (2.12)$$

Using this definition we see that,

$$\begin{aligned} \sigma_\Omega^{LO} &= \int dx_a dx_b d\mathbf{x} \delta(x_a x_b s - Q^2) \frac{f_i(x_a) f_j(x_b)}{x_a x_b s} \mathcal{B}_\Omega^{ij}(p_a, p_b, \mathbf{x}) . \\ &= \int d\mathbf{x} \mathcal{L}_{ij}(Q^2, x_l, x_u) \mathcal{B}_\Omega^{ij}(p_a, p_b, \mathbf{x}). \end{aligned} \quad (2.13)$$

This separation is convenient since  $\mathcal{B}_\Omega^{ij}(p_a, p_b, \mathbf{x})$  is Lorentz invariant and need only be evaluated for a single phase space point. The process independent integration over boosts is given by,

$$\begin{aligned} \mathcal{L}_{ij}(s_{ab}, x_l, x_u) &= \int dx_a dx_b \frac{f_i(x_a) f_j(x_b)}{x_a x_b s} \delta(x_a x_b s - s_{ab}) \\ &= \int_{x_l}^{x_u} dx_a \frac{f_i(x_a) f_j(s_{ab}/(s x_a))}{s x_a s_{ab}}, \end{aligned} \quad (2.14)$$

where in the second expression we have made the dependence on the upper and lower bounds explicit.

This factorisation in terms of initial and final state variables is exactly what we require to build our probability density function for the MEM since the experimental input is always a final state phase space point  $\mathbf{x}$ . We can define Eq. (2.1) more formally as,

$$\mathcal{P}(\mathbf{x}|\Omega) = \frac{1}{\sigma_{\Omega}^{LO}} \int d\mathbf{y} \mathcal{L}_{ij}(s_{ab}, x_l, x_u) \mathcal{B}_{\Omega}^{ij}(p_a, p_b, \mathbf{y}) W(\mathbf{x}, \mathbf{y}) . \quad (2.15)$$

For a completely inclusive description of the final state, Eqs. (2.14) and (2.15) are sufficient. However, realistic applications require transverse momentum and pseudo-rapidity cuts in order to define fiducial regions of the detector. It is therefore useful to consider the forms of the lab frame transverse momentum ( $p_T^{lab}$ ) and pseudo-rapidity ( $\eta^{lab}$ ) under the application of a given longitudinal boost parameterized by  $x_a$ .

The four-momenta of all the particles depend on the boost parameter – the initial state momenta  $p_a(x_a)$ ,  $p_b(x_a)$  and the momentum of particle  $i$  in the final state,  $p_i(x_a)$ . However we note that invariant masses,  $s_{ij} = 2p_i(x_a) \cdot p_j(x_a)$  cannot depend on the boost and may therefore be evaluated using any choice of boost parameter. The lab frame transverse momentum and pseudo-rapidity are defined in terms of such invariants and the boost parameter  $x_a$  by,

$$p_T^{lab,i} = \sqrt{\frac{s_{ai}s_{ib}}{s_{ab}}} , \quad \eta^{lab,i} = \frac{1}{2} \log \left( \frac{x_a^2 s_{ib}}{s_{ab} s_{ai}} \right) . \quad (2.16)$$

From these equations we see that  $p_T^{lab,i}$  does not depend on the boost parameter and therefore cuts on this quantity can be performed outside the boost integration, i.e. in Eq. (2.15). On the other hand,  $\eta^{lab,i}$  depends on  $x_a$ , so that cuts on the lab frame pseudo-rapidity should be included in Eq. (2.14). These cuts constrain the range of allowed boosts, i.e. the integration limits  $x_l$  and  $x_u$  are fixed by  $|\eta_{max}|$ .

In summary, by boosting an event to a frame in which the final state is  $p_T$ -balanced we have recovered Born kinematics and can assign a likelihood to the event uniquely. Frequently in the next sections we will refer to these frames, in which the Born event is well defined, as the “MEM frame”. As we have discussed, this definition is only unique in the transverse plane and the “MEM frame” is actually a set of equivalent frames connected by longitudinal boosts.

For the remainder of the paper we will make a simplification by assuming a “perfect” detector, i.e. the transfer function is equal to  $W(\mathbf{x}, \mathbf{y}) = \delta(\mathbf{x} - \mathbf{y})$ . This assumption is only valid for well-measured final state particles such as leptons and therefore as examples we only consider  $ZZ \rightarrow 4\ell$  and  $Z \rightarrow \ell^+\ell^-$ . We stress that non-trivial transfer functions do not pose any conceptual problems for our method and only entail additional integrations. Taking this simplification and the integration over the longitudinal boost into account, Eq. (2.15) becomes,

$$\mathcal{P}(\mathbf{x}|\Omega) = \frac{1}{\sigma_{\Omega}^{LO}} \mathcal{L}_{ij}(s_{ab}, x_l, x_u) \mathcal{B}_{\Omega}^{ij}(p_a, p_b, \mathbf{x}) . \quad (2.17)$$

The above equation defines the LO probability density function for the MEM. We recall that  $\mathcal{B}_{\Omega}^{ij}(p_a, p_b, \mathbf{x})$  represents the Born Matrix element squared,  $|\mathcal{M}_{\Omega}^{ij,(0)}(p_a, p_b, \mathbf{x})|^2$  and that



$\sigma_\Omega$  represents the fiducial cross section, calculated using cuts in the lab frame. We define the following quantity,

$$B_\Omega(\mathbf{x}) = \mathcal{L}_{ij}(s_{ab}, x_l, x_u) \mathcal{B}_\Omega^{ij}(p_a, p_b, \mathbf{x}) , \quad (2.18)$$

and observe from Eq. (2.13) that  $\int d\mathbf{x} B_\Omega(\mathbf{x}) = \sigma_\Omega^{LO}$ . We can thus simplify Eq. (2.17) to,

$$\mathcal{P}(\mathbf{x}|\Omega) = \frac{1}{\sigma_\Omega^{LO}} B_\Omega(\mathbf{x}). \quad (2.19)$$

This formalism will prove useful in the following section when we extend the MEM to NLO.

Using the techniques outlined above we have defined a procedure that takes an observed final state,  $\tilde{Q} + X$  and relates it to a LO model for the process,  $p_a + p_b \rightarrow Q$ . Specifically, given an arbitrary amount of additional radiation we create a phase space point that recovers the Born kinematics, at the cost of introducing an integration over the longitudinal degree of freedom.

Clearly this model will be better for events in which the momentum imbalance  $X$  is small, rather than events in which  $X$  is kinematically relevant, i.e. in the presence of one or more additional jets. When additional jets are present one has three options. The first option is to simply apply the LO model presented above, boosting the jet into the initial state. Since in general one expects this method to be rather sensitive to the amount of radiation, i.e. the transverse momentum of the jet, it is prudent to check the validity of this approach by also considering smaller data sets obtained by applying a jet veto. If there are sufficient events, restricting the data set by imposing a strict jet veto is preferred since, by ensuring that no additional hard jets are present, one can be confident that the LO model works reasonably well. We shall present an example of applying such a jet veto in section 4. The second option is to use a LO calculation that already contains an additional jet, i.e.  $p_a + p_b \rightarrow Q + \text{jet} + X$ . In this case the extra radiation is well modelled but the MEM must be extended to include a systematic treatment of jets. In this paper we will not consider this option further.

Finally, one may try to systematically improve the MEM in an attempt to model the additional radiation. This is the approach discussed in Ref. [36], with reference to initial state radiation. Instead one may incorporate such effects by extending the MEM to NLO. Since a NLO calculation includes the radiation of one additional parton, a first approximation of the effects of further radiation is made at this order. In the next section we will illustrate how this may be achieved within the MEM framework.

### 3. The Matrix Element Method at Next-to-Leading Order

In this section we define the MEM at NLO and, as a by-product, discuss how one may generate unweighted events at NLO.

#### 3.1 Going beyond LO: Defining NLO on an event by event basis

The goal of this sub-section is to illustrate how to extend the MEM to NLO in perturbation theory. However this is not a simple task since in a normal NLO calculation virtual

and bremsstrahlung events live in separate phase spaces, their only communication being through a regularising subtraction scheme. Instead of following this procedure, we need to reorganise the calculation such that it can provide a NLO weight for a given Born event, with the sum over the event weights recovering the usual NLO cross section. To do this we begin by assuming that our event has been rendered in the MEM frame using the procedure described in the previous section. We note however that the procedure we will outline in this section is not useful solely for extending the MEM to NLO. We are creating a method for producing a NLO cross section from a series of Born phase space points, a procedure that may have broader applications than are presented here.

Given the phase space point  $\mathbf{x} = p_1, \dots, p_n$  where the final state momenta are those of the identified final state particles, we can define the NLO corrections by,

$$\frac{d\sigma_{\Omega}^{NLO}(\mathbf{x})}{d\mathbf{x}} = R_{\Omega}(\mathbf{x}) + V_{\Omega}(\mathbf{x}) . \quad (3.1)$$

This follows the usual separation of the NLO calculation into two pieces, each of which is associated with a different phase space. We stress though that here the separation has been performed for a fixed Born phase space point,  $\mathbf{x}$ . The definition of the term associated with the virtual corrections is straightforward since it is defined in the same phase space as the Born contribution. Explicitly, we can define  $V_{\Omega}(\mathbf{x})$  as,

$$\begin{aligned} V_{\Omega}(\mathbf{x}) = & \mathcal{L}_{ij}(s_{ab}, x_l, x_u) \left( \mathcal{B}_{\Omega}^{ij}(p_a, p_b, \mathbf{x}) + \mathcal{V}_{\Omega}^{ij}(p_a, p_b, \mathbf{x}) \right) \\ & + \sum_{m=0}^2 \int dz \left( \mathcal{D}_m(z, \mathbf{x}) \otimes \mathcal{L}_m(z, s_{ab}, x_l, x_u) \right)_{ij} \mathcal{B}_{\Omega}^{ij}(p_a, p_b, \mathbf{x}). \end{aligned} \quad (3.2)$$

Here the first term represents the combination of the Born matrix element  $\mathcal{B}_{\Omega}^{ij}$  and the one-loop Born interference term  $\mathcal{V}_{\Omega} = 2\text{Re}|\mathcal{M}_{\Omega}^{(0)*} M_{\Omega}^{(1)}|$  (where the dependence on the initial state partons has been suppressed). This is coupled to the same boost function,  $\mathcal{L}_{ij}$  as was defined at LO. In our approach we have followed the NLO implementation of MCFM and used the dipole subtraction procedure of Catani and Seymour [37] to handle the singularities in the virtual and real calculations. The final term in Eq. (3.2) contains the integrated subtraction terms,  $\mathcal{D}_a$ , introduced in this formalism. Since we are considering initial state singularities the integrated dipoles depend on a convolution variable  $z$ . This variable is convoluted with the boost function to create three structures,

$$\mathcal{L}_0 = \mathcal{L}, \quad \mathcal{L}_1 = \int_{x_l}^{x_u} dx_a \frac{f_i(x_a/z) f_j(s_{ab}/(zx_a))}{z s x_a s_{ab}}, \quad \mathcal{L}_2 = \int_{x_l}^{x_u} dx_a \frac{f_i(x_a) f_j(s_{ab}/(z s x_a))}{z s x_a s_{ab}}. \quad (3.3)$$

In Eq. (3.2) the sum over these convolutions is given by  $m$ .

Using Eq. (3.2) we are able to define an event by event finite weight associated with the Born plus virtual contributions. Our remaining task is thus to define  $R_{\Omega}(\mathbf{x})$  such that there is no double counting of events. In other words we must ensure that the integration of Eq. (3.1) results in the total NLO cross section ( $\sigma_{\Omega}^{NLO}$ ). One way to ensure this is to

use a forward branching phase space generator (FBPS) [38] to construct the real phase space. Starting from the Born phase space point,  $\hat{p}_a + \hat{p}_b \rightarrow Q$  the FBPS generates the real radiation by branching one of the initial state momenta to produce the real phase space point  $p_a + p_b \rightarrow Q + p_r$ . In the following we will use the hatted notation to indicate a Born phase space point, whilst the un-hatted momenta represent the real phase space point.

The phase space generator needs to integrate out all initial state radiation within the constraints of fixed momenta of the identified final state particles (and, if required, the jet veto). We show in Appendix A that this can be achieved using a FBPS generator defined by,

$$d\Phi(p_a + p_b \rightarrow Q + p_r) = d\Phi(\hat{p}_a + \hat{p}_b \rightarrow Q) \times d\Phi_{\text{FBPS}}(p_a, p_b, p_r) \times \theta_{\text{veto}} , \quad (3.4)$$

where  $\theta_{\text{veto}}$  (optionally) vetoes events that generate an additional jet. At NLO the jet veto cut is simply,

$$\theta_{\text{veto}}(p_r) = \theta \left[ p_T^{\text{lab}}(p_r) < p_T^{\text{min}}(\text{jet}) \right] , \quad (3.5)$$

where  $p_T^{\text{lab}}(p_r)$  is the laboratory frame transverse momentum (calculated using Eq. (2.16)). Note the initial state brancher is necessarily an antenna brancher since it ensures that the initial state partons remain massless. The form of the FBPS generator, in terms of the kinematic variables  $p_a$ ,  $p_b$  and  $p_r$ , is,

$$d\Phi_{\text{FBPS}}(p_a, p_b, p_r) = \frac{1}{(2\pi)^3} \left( \frac{\hat{s}_{ab}}{s_{ab}} \right) dt_{ar} dt_{rb} d\phi , \quad (3.6)$$

where  $t_{xy} = (p_x - p_y)^2$  and  $d\phi$  is a rotational degree of freedom about the  $z$ -axis. The explicit construction of the momenta  $p_a$ ,  $p_b$  and  $p_r$  in terms of the integration variables is detailed in Appendix A. The phase space weight corrects the flux factor due to the resulting emission of an extra parton.

Finally, we observe that the forward brancher must by necessity change the initial state momenta. This means that for bremsstrahlung events the values of  $p_T^{\text{lab}}$  will depend on the branching momentum  $p_r$ . Thus although the four momenta of the final state particles are fixed in the MEM frame the value of the  $p_T^{\text{lab}}$  observable changes dynamically. In other words a single event with fixed MEM frame four momenta corresponds to a range of  $p_T^{\text{lab}}$  values. Using the FBPS we can now explicitly define  $R_\Omega(\mathbf{x})$  as,

$$R_\Omega(\mathbf{x}) = \int d\Phi_{\text{FBPS}}(p_a, p_b, p_r) \left( \mathcal{L}_{ij}(s_{ab}, x_l, x_u) \mathcal{R}_\Omega^{ij}(p_a, p_b, \mathbf{x}, p_r) - \sum_m \mathcal{L}_{ij}(s_{ab}, x_l^m, x_u^m) D^m(p_a, p_b, p_r) \mathcal{B}_\Omega^{ij}(\hat{p}_a, \hat{p}_b, \mathbf{x}) \right). \quad (3.7)$$

In the above we note that the boost integral is defined for a given branching, since each branching generates a new  $s_{ab}$ . The quantity  $\mathcal{R}_\Omega^{ij}(p_a, p_b, \mathbf{x}, p_r) = |M_\Omega^{(0)}(p_a, p_b, \mathbf{x}, p_r)|^2$  is the Born level matrix element with one additional parton. Finally,  $D(p_a, p_b, p_r) \mathcal{B}_\Omega^{ij}(\hat{p}_a, \hat{p}_b, \mathbf{x})$  represents the subtraction terms that cancel the soft and collinear divergences which occur when  $p_r$  is unresolved. A couple of observations are in order in regards to the dipole pieces. We note that, since the dipoles must provide a pointwise cancellation, the boost function inherits the same  $s_{ab}$  as in the real boost function. However the underlying Born

matrix element must be evaluated using the original Born  $\hat{s}_{ab}$  in order to have a one-to-one correspondence with Eq. (3.2). This also fixes the integration limits,  $x_l^m$  and  $x_u^m$  in Eq. (3.7). We discuss the exact modifications to the usual dipole subtraction scheme in Appendix B.

We are now in a position to build our scattering probability accurate to NLO, based on the quantities  $V_\Omega(\mathbf{x})$  and  $R_\Omega(\mathbf{x})$  that we have defined in Eqs. (3.2) and (3.7) above. The NLO probability density function associated with the event  $\mathbf{x}$  is,

$$\mathcal{P}(\mathbf{x}|\Omega) = \frac{1}{\sigma_\Omega^{NLO}} \left( V_\Omega(\mathbf{x}) + R_\Omega(\mathbf{x}) \right). \quad (3.8)$$

This equation defines the MEM at NLO.

### 3.2 Generating unweighted events at NLO

A welcome by-product of the method outlined in the previous sub-section is its ability to generate unweighted events at NLO. In this section we outline how this is possible and in later sections we will use the technique to generate samples of unweighted events that can be used to test the MEM.

Our starting point is Eq. (3.1), in which we explicitly separated the NLO calculation into real and virtual contributions. We define the inclusive phase space spanned by the Born processes as  $\Phi$ , which we can separate into two regions. Region I is the part of the inclusive phase space,  $\Phi$ , that is populated by the LO calculation under the lab frame cuts. Region II is the remaining part of the inclusive phase space, in which the LO calculation does not contribute.

We focus first on region I. Since the LO contribution is non-zero we can write a point by point  $K$ -factor as follows,

$$\begin{aligned} K_I(\mathbf{x}) &= \frac{d\sigma^{NLO}}{d\mathbf{x}} \left( \frac{d\sigma^{LO}}{d\mathbf{x}} \right)^{-1} \\ &= \frac{V_\Omega(\mathbf{x}) + R_\Omega(\mathbf{x})}{B_\Omega(\mathbf{x})}. \end{aligned} \quad (3.9)$$

This quantity is not positive definite since one can construct phase space points for which  $K_I(\mathbf{x}) < 0$ . However, these correspond to regions in which the NLO calculation is unphysical. More specifically, it is possible to choose a renormalisation scale such that the differential cross section becomes negative. Typically this occurs because the choice of renormalisation scale is widely separated from the typical scale of the event. In general if a sensible scale choice is used then  $K_I(\mathbf{x}) > 0$ . In order to ensure that  $K_I(\mathbf{x}) > 0$  it is sufficient to check that the NLO differential cross section is positive in all observables. One can then create weighted NLO events in this region by generating a Born phase space point and recording both the Born weight,  $B_\Omega(\mathbf{x})$  and the  $K$ -factor,  $K_I(\mathbf{x})$  for that point (as well as the phase space weight associated with  $\mathbf{x}$ ). If the calculation is completely inclusive, i.e. no cuts are applied and region II is empty, then an unweighted NLO sample can easily be obtained by unweighting the combination of  $K_I(\mathbf{x})$ ,  $B_\Omega(\mathbf{x})$  and the phase space weight.

In region II there is no  $K$ -factor since the LO cross section is zero. In this region the virtual contribution, and all of the terms associated with the subtraction procedure, are zero since they occupy the Born phase space. Hence  $K_{II}(\mathbf{x})$  is positive definite since it only corresponds to the LO process with an additional parton,

$$K_{II}(\mathbf{x}) = R_{\Omega}(\mathbf{x}) . \quad (3.10)$$

Therefore in region II we construct our weights as a combination of the phase space weight associated with  $\mathbf{x}$  and  $K_{II}(\mathbf{x})$ .

By combining regions I and II we have weights that span the entire phase space and which are positive (with the caveat that the total NLO differential cross section should be positive everywhere). Although the events all have the structure of a Born phase space point, the sum over the associated weights results in the NLO cross section. We stress that the events found in region II are those in which the Born contribution is zero due to fiducial cuts and not a kinematic cut off. For example if one demanded a leptonic  $p_T$  cut of 15 GeV then region II would correspond to  $p_T < 15$  GeV. On the other hand, if the lepton had some natural cut off (for example,  $p_T > m_Z/2$ ) then this region is already excluded from the inclusive Born phase space,  $\Phi$ . Using the weighted sample described here one can produce unweighted events in exactly the same fashion as one does at LO.

## 4. Validation

In this section we present a simple validation of the method outlined in the previous section, focussing for simplicity on the production of lepton pairs at the LHC,  $pp \rightarrow Z/\gamma^* \rightarrow \ell^+ \ell^-$ . In the first instance we study physics in the MEM frame, comparing predictions for observables in this frame with the more familiar ones obtained in the lab frame. For this exercise, we investigate parton level calculations (at LO and NLO) and Pythia [34]. The use of Pythia is a valuable test of our method since it contains the effects of a parton shower, underlying event and hadronisation in its output. After this study we present a simple comparison of the MEM method at LO and NLO, in the context of a  $Z$  mass measurement.

### 4.1 Physics in the MEM frame.

We begin by recalling the definitions of lab frame quantities ( $p_T$  and  $\eta$ ) that we use to apply cuts in the MEM frame,

$$p_T^{lab,i} = \sqrt{\frac{s_{ai}s_{ib}}{s_{ab}}} , \quad \eta^{lab,i} = \frac{1}{2} \log \left( \frac{x_a^2 s_{ib}}{s_{ab} s_{ai}} \right) . \quad (4.1)$$

In passing we note that, although it is not needed in the cases that we will discuss here, we can also easily define lab-frame azimuthal angle and rapidity differences in a boost-independent fashion,

$$\Delta\eta_{ij}^{lab} = \frac{1}{2} \log \left( \frac{s_{bi}s_{aj}}{s_{ai}s_{bj}} \right) , \quad \Delta\phi_{ij}^{lab} = \cos^{-1} \left( \cosh(\Delta\eta_{ij}^{lab}) - \frac{s_{ij}}{2p_T^{lab,i} p_T^{lab,j}} \right) . \quad (4.2)$$

These definitions would be useful for more complicated processes that include jets or that require the application of an isolation procedure. We will also consider the MEM frame transverse momentum, which is defined in a more familiar way,

$$p_T^{MEM,i} = \sqrt{(p_i^x)^2 + (p_i^y)^2}, \quad (4.3)$$

where, of course, the four-vector  $p^\mu$  is explicitly in the MEM frame. The MEM frame has no unique definition of pseudo-rapidity for a given event, since there are multiple frames connected by longitudinal boosts.

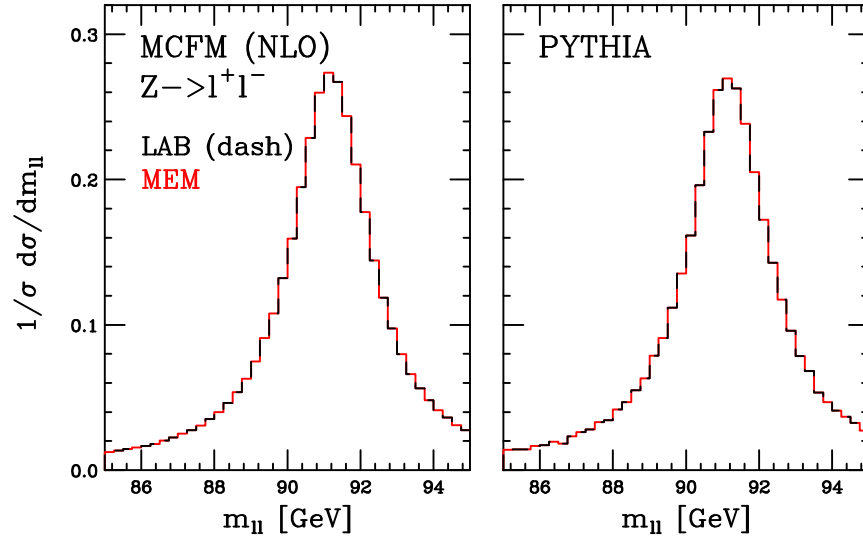
We now wish to study the behaviour of different quantities in the lab and MEM frames. We apply very loose cuts, namely we only require that the leptons lie in the invariant mass window,

$$80 \text{ GeV} < m_{\ell^+\ell^-} < 100 \text{ GeV}. \quad (4.4)$$

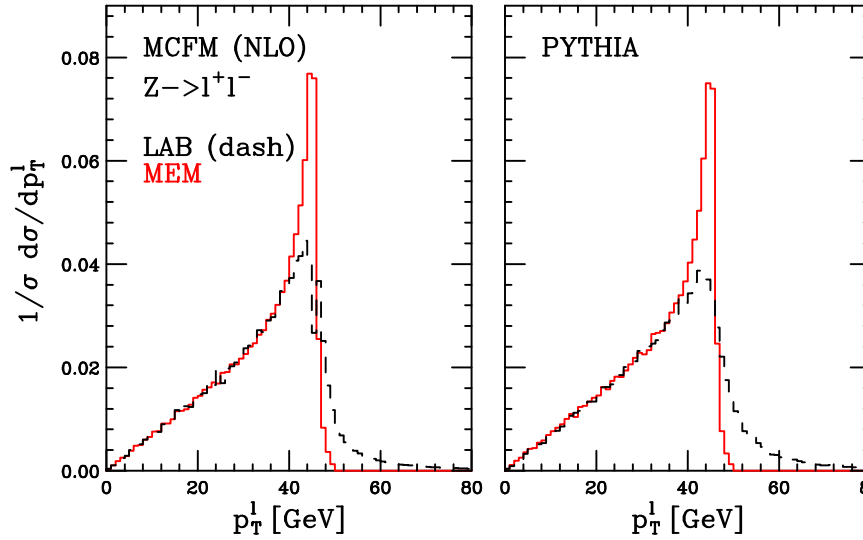
We generate LO and NLO parton level events using MCFM and more exclusive particle-level dilepton events using Pythia. In Fig. 2 we compare the results from the lab and MEM frames for the quantities  $p_T^{lab}$ ,  $p_T^{MEM}$  and  $m_{\ell\ell}$ .

In Fig. 2(a) we see that, as is necessary, the invariant mass of the lepton pairs is identical in both frames. A more interesting quantity is the frame-dependent  $p_T$  of the positively charged lepton,  $\ell^+$ , shown in Fig. 2(b). At LO (parton level) the two quantities are the same because for pure LO results the final state has zero net transverse momentum and thus the MEM and lab frames are identical. As soon as this simple picture is broken the two frames are no longer the same and the  $p_T$  distributions differ. This is apparent in both the showered and NLO results. For the NLO and shower predictions it is possible, by radiating additional particles, for a lepton to have lab-frame  $p_T$  greater than  $m_Z/2$ . At LO this is not kinematically accessible, modulo small width effects. This is demonstrated in the lab frame  $p_T$  predictions for the NLO and showered results, shown in Fig. 2(b), that produce a high  $p_T$  tail. The MEM frame, however, requires that the event be boosted back to a Born topology. As such, the high  $p_T$  region is not present in this frame. Since the overall normalisation is fixed by the total cross section these events are manifested at lower values of  $p_T$ , with the region around  $m_Z/2$  showing a considerable enhancement relative to the lab frame.

In Fig. 3 we directly compare the different theoretical predictions – at LO, NLO and using Pythia – in both the lab and MEM frames. It is clear that the predictions in the MEM frame are very similar with respect to each other, with both LO and Pythia predicting a slightly softer spectrum relative to NLO. We note that the shape differences between NLO and the other predictions is consistently of order 10% or less. In the lab frame, however, there are significant differences between the predictions, in particular in the region  $p_T > m_Z/2$ . From this discussion we conclude that the MEM frame possesses some very nice features. In particular the differences with respect to the LO prediction (from either shower or NLO) are consistent with naive estimates of higher order QCD effects, suggesting good perturbative control. The main reason for the convergence is that, in the MEM frame, kinematic ranges of observables are not extended beyond their LO



(a)



(b)

**Figure 2:** Comparison between the lab and MEM frame predictions from the NLO calculation of MCFM (left) and Pythia (right) for the process  $pp \rightarrow Z/\gamma^* \rightarrow \ell^+ \ell^-$ . In (a) we plot the invariant mass distribution of the two leptons and in (b) we show the  $p_T$  of the positively charged lepton. In each plot the lab frame quantity is shown in black (dashed), while the MEM frame result is in red (solid).

boundaries. Since any such extension beyond the LO region is necessarily sensitive to further higher order corrections, the elimination of this aspect of the calculation should be seen as an advantage for the MEM frame.

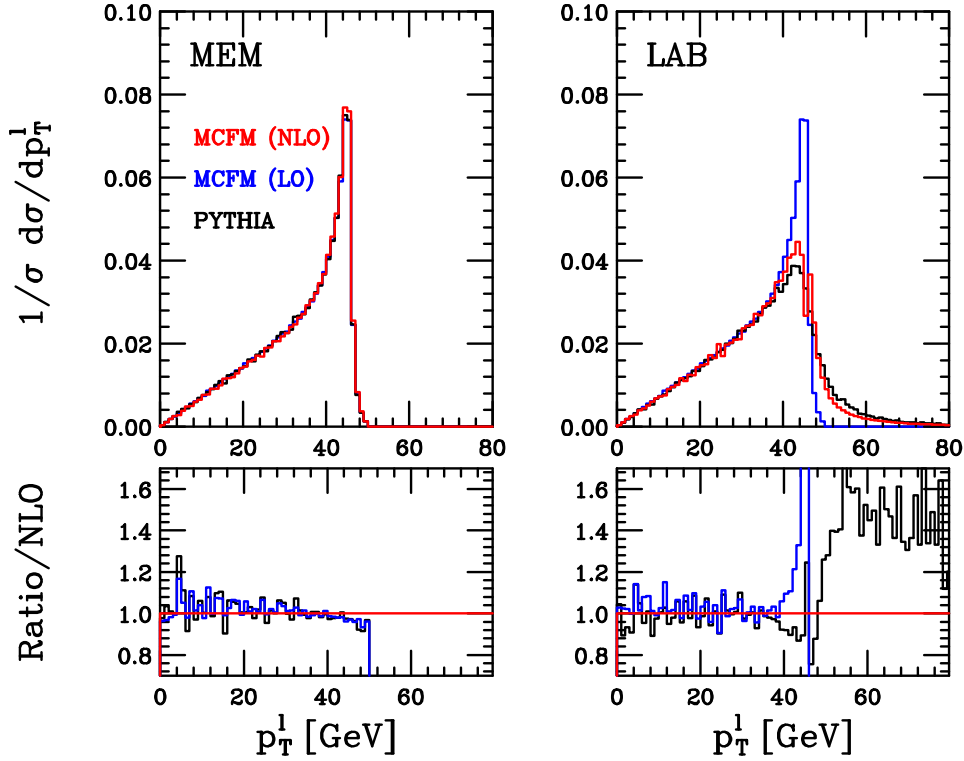


**Figure 3:** Comparison between MCFM (LO and NLO) and Pythia in different frames. On the left hand side  $p_T^\ell$  is plotted in the MEM frame, whilst on the right hand side the lab frame equivalent is plotted. Predictions are normalised by the total cross section (or number of events in the Pythia case).

#### 4.2 Validating the MEM: measuring $m_Z$

In the previous sub-section we have used MCFM, representing a traditional approach to NLO calculations, to generate lab frame events that are then transformed into the MEM frame. As described in the previous section, for the extension of the MEM method to NLO it is easiest to work directly in the MEM frame. We have modified MCFM accordingly to incorporate the phase space generator and approach described in the previous section. In addition to the implementation of the FBPS, the code has been constructed such that a NLO weight can be ascribed to an individual event in the MEM frame.

A simple test of our implementation of the MEM at LO and NLO is its application to the measurement of the mass of the  $Z$  boson at the 7 TeV LHC. To this end we generate  $\mathcal{O}(5000)$  events using Pythia that satisfy the following lab frame requirements,

$$p_T^\ell > 15 \text{ GeV} , \quad |\eta_\ell| < 2.5 , \quad 80 \text{ GeV} < m_{\ell+\ell^-} < 100 \text{ GeV}. \quad (4.5)$$

We use Pythia since it is a completely independent code to MCFM and as such is also independent of our new method for generating the NLO weights. In addition, Pythia output is at the particle level, including shower, hadronisation and underlying event models. We note that in Pythia we have turned off both the mass of the leptons and QED radiation,



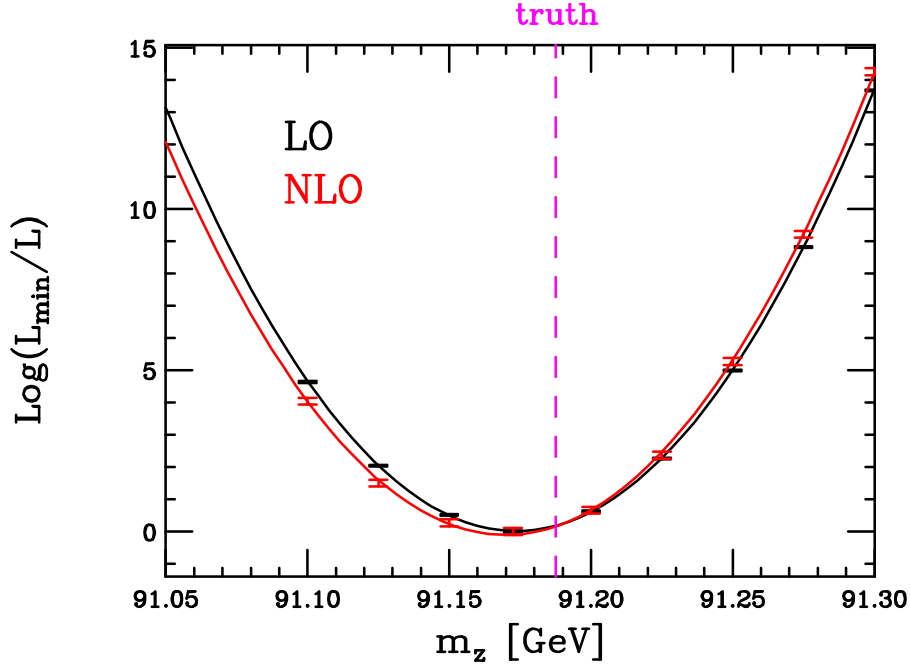


**Figure 4:** Log-likelihoods obtained by a MEM analysis at LO (black) and NLO (red) for the measurement of  $m_Z$  at the LHC using Pythia data. Errors represent MC integration uncertainty.

both of which ensure our transfer function assumptions remain valid. In Fig. 4 we present the likelihoods as a function of  $m_Z$  for the completely inclusive case (i.e. the full data set). As expected we observe a parabolic function around the best fit mass. Error bars represent the Monte Carlo integration uncertainty and statistical uncertainties can be inferred by using Eq. (2.4). We observe that the truth value ( $m_Z = 91.1876$  GeV) easily lies within the  $1\text{-}\sigma$  band of our best fit values,

$$\text{LO: } m_Z = 91.170 \pm 0.025 \text{ GeV} \quad \text{NLO: } m_Z = 91.174 \pm 0.025 \text{ GeV} . \quad (4.6)$$

The power of the MEM is also illustrated here, since with a data set of  $\mathcal{O}(0.1)$  fb $^{-1}$  we are able to perform a measurement of the  $Z$  mass to within 25 MeV (modulo transfer function uncertainties). It is not surprising that the NLO and LO results are very close to one another since we have already observed that, for this process, the NLO and LO kinematics are very similar in the MEM frame.

The results presented in Fig. 4 are for the full sample that includes events in which there is a significant amount of showered radiation. Since there is no model of this additional radiation in the LO MEM, one may worry that the measured value of  $m_Z$  depends on the amount of this additional radiation. We therefore present the results of a study of this effect in Fig. 5, where we have performed the mass measurement for a variety of cuts on the transverse momentum of the dilepton ( $Z$ ) system,  $p_T^{\ell\ell}$ . By varying the maximum value of this quantity for events in our sample, we are limiting the amount of additional radiation (i.e. showering) present in the event. Since this veto represents an additional cut on the data, the size of the data sample shrinks as the maximum  $p_T^{\ell\ell}$  is reduced. For this reason the

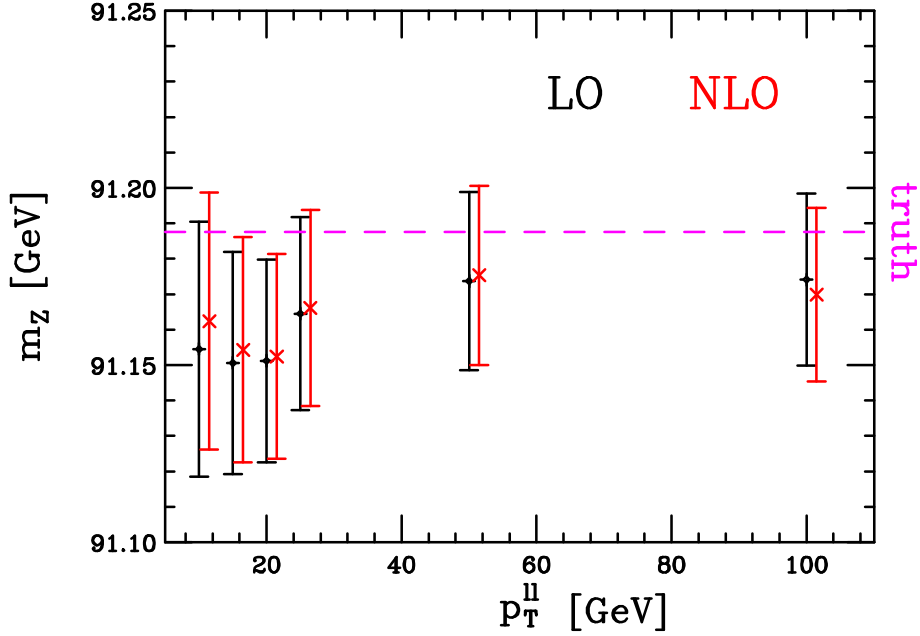


**Figure 5:** Reconstructed  $Z$  mass as a function of the upper bound on the transverse momentum of the dilepton system,  $p_T^{\ell\ell}$ . Errors represent the  $1\sigma$  deviation from the central value. Note that both LO and NLO calculations are performed at the same values of the cut,  $p_T^{\ell\ell}$ . In the plot the NLO points have been moved slightly to the right for clarity.

statistical uncertainty increases at low  $p_T^{\ell\ell}$ , as is apparent from the uncertainties shown in the figure. For this observable it is clear that both the dependence on the boost and on the higher order corrections is small. The relative independence of the results from the amount of shower radiation allowed in the events illustrates that the boost method has worked well for this observable. This is encouraging but should not be taken as a general rule for all observables. The boost changes the parton fractions  $x_a$  and  $x_b$  and thus observables that are sensitive to such changes will become dependent on the amount of additional radiation in the event. In cases where imposing a jet veto is desirable, the boost (in)dependence should be checked by performing the measurement with a desired veto, and recalculating the observable with a tighter veto upon the same data set. If the two results agree within statistical errors then one is reassured that the shower is playing a minimal role. One may expect that, given its improved modeling of additional radiation, that the NLO results will be less sensitive to the additional radiation.

## 5. The Higgs Boson search in the channel $H \rightarrow ZZ \rightarrow 4\ell$

A convenient example in which to test our MEM implementation at LO and NLO is the Higgs search at the LHC. One of the cleanest search channels is the process  $H \rightarrow ZZ \rightarrow 4\ell$  [39, 40] since the final state can be fully reconstructed in the detector and the SM backgrounds are small. With full control of the final state, with no sizeable missing transverse momentum or jet activity expected, this channel is a natural candidate for a

MEM approach. The use of the MEM in this channel has been studied in some detail in ref. [41], with the usual caveat of the leading order limitation. Since the NLO corrections to this process are large it is interesting to determine whether the MEM at NLO can improve upon the LO analysis.

### 5.1 Event selection

In the following examples we will select events that contain four leptons satisfying the following requirements,

$$\begin{aligned} p_T^{\ell_1, \ell_2} > 20 \text{ GeV} , \quad p_T^{\ell_3, \ell_4} > 5 \text{ GeV} , \quad |\eta_\ell| < 2.0 , \\ 15 \text{ GeV} < m_{\ell\bar{\ell}} < 115 \text{ GeV} , \quad 75 \text{ GeV} < m_{\ell'\bar{\ell}'} < 115 \text{ GeV} , \end{aligned} \quad (5.1)$$

where leptons are labelled in order of decreasing transverse momentum from  $\ell_1$  to  $\ell_4$ . That is, we require one pair of oppositely-charged leptons to have an invariant mass within approximately 15 GeV of the  $Z$  mass while the invariant mass of the other pair is less constrained. In experimental searches the analysis cuts are typically tailored to the putative Higgs mass in order to better discriminate against the relevant backgrounds. However, for simplicity, in our studies we do not optimise the cuts in this way. Therefore the limits and uncertainty ranges quoted here should be taken only as a rough estimate of what can be achieved in a true experimental analysis. Instead, we are more interested in assessing the performance of the MEM at LO and NLO for a given set of cuts.

We perform our calculation for the LHC operating at  $\sqrt{s} = 7 \text{ TeV}$ , with  $\mu_R = \mu_F = m_H$  in the calculation of the Higgs signal and  $\mu_R = \mu_F = 2m_Z$  for the  $ZZ$  background. We have used the MSTW2008 PDF set [42] matched to the appropriate order in perturbation theory. Our NLO calculation includes the contributions from  $gg \rightarrow ZZ$  for  $n_f = 5$  massless flavours, using results taken from MCFM [32]. Although the interference between SM production of  $WW$  pairs and the Higgs signal may be phenomenologically relevant [43], in the  $ZZ \rightarrow 4\ell$  channel the corresponding interference is not expected to be important for a light Higgs boson since the final state is fully reconstructed. Although the interference effects may become non-negligible for Higgs masses above a few hundred GeV, we do not include such effects here.

### 5.2 Higgs mass limits in the absence of the signal process

We begin by studying the scenario in which there is no Higgs boson and the only source of four lepton events is  $pp \rightarrow ZZ \rightarrow 4\ell$  production, i.e. neglecting any other source of backgrounds. We therefore expect to set limits on the SM Higgs, which we can do by defining one- and two-sigma confidence limits on its mass. As an illustrative example we choose to keep our definition of these contours from the Gaussian definition given in the previous section. Since the main thrust of this work is the study of the differences between LO and NLO MEM analyses, the exact definition of these limits is not crucial to our conclusions.

We study the MEM using event samples that are generated at NLO parton level. Hadronic production of a Higgs boson through the gluon fusion mechanism is known to

have large  $K$ -factors associated with higher order corrections. In this instance this is also true of the continuum background. The size of the gluon flux at the LHC also results in the  $gg$ -initiated contributions contributing at the order of 10% of the total. Since MCFM [32] includes all these effects and is known to model the shape of the four lepton invariant mass distribution reasonably well [39], we expect that a NLO parton level simulation should give a reasonably realistic description of the most important features of actual four lepton events. We use the procedure outlined at the end of section 3 to directly generate NLO unweighted events in the MEM frame, where each of these events has the kinematic structure of a Born phase space point. We note that some of these events possess leptons with, for instance,  $p_T^{MEM, \ell_4} < 5$  GeV. Since, at LO,  $p_T^{MEM} = p_T^{lab}$  these events cannot pass the fiducial cuts in the LO analysis and as such are not included in the calculation of the likelihood. However, at NLO, the transverse momentum is not identical in the two frames,  $p_T^{MEM} \neq p_T^{lab}$ . Therefore a value of  $p_T^{MEM} < 5$  GeV can correspond to a real radiation contribution with  $p_T^{lab} > 5$  GeV. As a result such events are included in the NLO likelihood calculation. Therefore there can be a different number of events in the LO and NLO data samples. This is a reflection of the fact that the NLO calculation exhibits a richer kinematical structure than the LO one.

We generate 253 NLO background events,  $pp \rightarrow ZZ \rightarrow 4\ell$ , that pass the cuts given in Eq. (5.1) and then perform a MEM analysis at both LO and NLO. Due to the issue discussed above, only 250 of these enter the LO calculation. Our results are shown in Figure 6, where we present results as log-likelihood differences,  $\log(L_B/L_{S+B})$ . The likelihoods are for a signal plus background hypothesis for a given Higgs mass ( $L_{S+B}$ ), and for a hypothesis in which there is background only ( $L_B$ ). If a Higgs boson at a given  $m_H$  is more probable than the background only hypothesis then the resulting difference is negative. However if the Higgs signal is less favourable than the background only hypothesis then this quantity is positive. Therefore a larger difference with respect to zero results in a stronger signal or more stringent limits. Since our sample was generated without a Higgs boson signal (and no chance fluctuations mimicking a signal) we observe that the difference is always positive. We can then proceed to set limits at the 1- and 2- $\sigma$  levels by requiring that  $\log(L_B/L_{S+B}) > 1/2$  and  $\log(L_B/L_{S+B}) > 2$  respectively. With these definitions we find the following 95% confidence exclusion range at LO,

$$\text{LO MEM exclusion:} \quad 120 \text{ GeV} < m_H < 380 \text{ GeV} , \quad (5.2)$$

while the NLO MEM provides the more stringent exclusion limit,

$$\text{NLO MEM exclusion:} \quad 100 \text{ GeV} < m_H < 430 \text{ GeV} . \quad (5.3)$$

Although these limits are an interesting example of the MEM at LO and NLO, we remind the reader that they should not be taken too literally. In particular we have not modified the selection cuts as a function of  $m_H$ , for instance to use more efficient cuts in the heavy Higgs region that better maximise the signal/background ratio. In that scenario one would be better able to discriminate between signal and background and the presence (or lack) of Higgs signal events would result in stronger limits (or greater significance of a discovery).

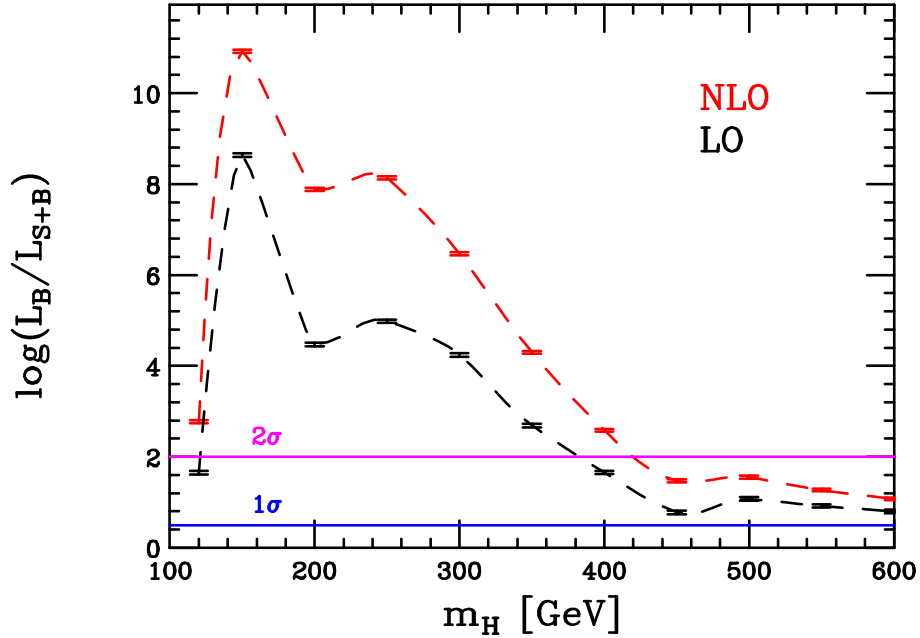


**Figure 6:** The log-likelihood difference for background only and signal plus background, for a Higgs boson search in the channel,  $H \rightarrow ZZ^* \rightarrow 4$  leptons. Positive values of the difference indicate that the background-only hypothesis is more likely than the signal plus background one. The blue and magenta lines represent the 1- and 2- $\sigma$  limits respectively.

In section 5.5 we will present a more detailed study, involving the generation of many pseudo-experiments, in order to investigate the true potential for setting limits on the Higgs boson mass by using the MEM at LO and NLO. We also note that in this section we are using NLO data and therefore the fact that NLO gives stronger limits is hardly surprising. However under the assumption that the data is better modelled by a NLO prediction than a LO one, we can infer that the NLO MEM might give better results than its LO counterpart.

### 5.3 Results in the presence of a Higgs boson with $m_H = 125$ GeV

We now consider the case in which the SM Higgs exists and has a mass  $m_H = 125$  GeV. We use the same background events and cuts as in the previous section and include in addition three Higgs signal events that are generated from an unweighted NLO sample.

For this mass the SM Higgs is a very narrow resonance,  $\Gamma_H = 0.417 \times 10^{-2}$  GeV, and as a result the MEM might be expected to measure the mass very precisely even with only a few events. This is indeed what we observe in our results, shown in Fig. 7. The curves, both at LO and NLO, exhibit a very sharp valley at  $m_H = 125$  because each unweighted signal event has almost exactly the same mass due to the tiny width. A handful of events clustered at a single mass, in this case  $m_H = 125$  GeV, is clearly a very significant feature. In this example one signal event has  $p_T^{MEM, \ell_4} = 3.8$  GeV and, as already discussed, therefore fails the cuts in the LO MEM analysis. However, the remaining 3 leptons in this

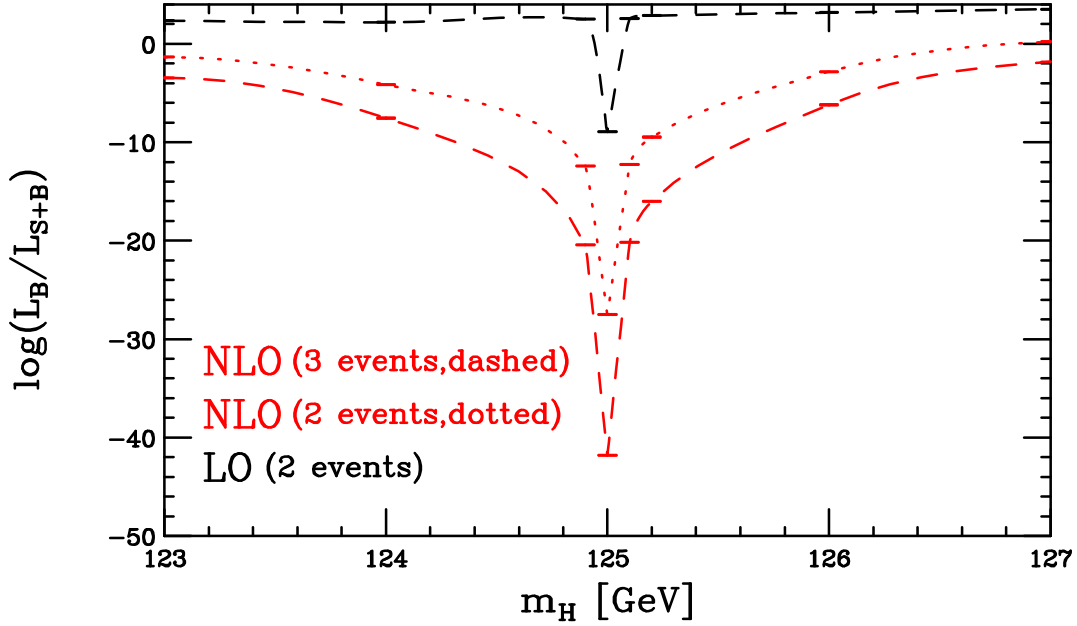


**Figure 7:** Log likelihoods for a light Higgs boson decaying into four leptons, where we have injected a signal at  $m_H = 125$  GeV. The dashed lines indicate the results obtained when including all 3 signal events at NLO. The dotted line represents the NLO likelihood when the event that fails the cuts in the LO analysis is omitted.

event have larger transverse momenta, thus allowing real radiation contributions to provide a contribution to the NLO likelihood. This enhances the differences between LO and NLO since the overall sample size is so small. In order to quantify the impact of the event that fails the cuts at LO, we present the NLO results obtained when omitting this event as a dotted curve in Fig. 7. We observe that the peak value is reduced by about a third, indicating that although this event fails the LO cuts, it still possesses a non-negligible weight that the NLO calculation is able to utilise. The remaining large difference between LO and NLO can be understood by considering the physics in the region around  $m_{4\ell} \sim 125$  GeV. As a result of our cuts there are very few background events, which means that the log-likelihood difference is more sensitive to the large signal  $K$ -factor than in regions in which the background is sizeable. In other words, since the  $K$ -factor for the background is also large, regions in which background events occur frequently tend to spoil the NLO enhancement of the signal in the likelihood difference.

In both LO and NLO cases, the MEM can measure the mass much better than the expected experimental resolution from the transfer functions. That is, we have stretched our assumption that  $W(\mathbf{x}, \mathbf{y}) = \delta(\mathbf{x} - \mathbf{y})$  well beyond its expected validity. Clearly, a trustworthy assessment of the accuracy of a MEM element approach in this scenario must be performed using a more sophisticated experimental analysis, which is beyond the scope of this work. We note that if the transfer functions can be determined sufficiently accurately (say from Drell-Yan events) then the MEM will most likely provide the best measurement of the Higgs mass in this channel. In addition the MEM should be very useful in the future

study of the light Higgs, i.e. by probing its couplings and spin. We leave such a study to future work.

#### 5.4 Results in the presence of a Higgs boson with $m_H = 425$ GeV

Finally we consider the case of a heavier Higgs boson ( $m_H = 425$  GeV), that is consequently much broader,  $\Gamma_H = 37.6$  GeV. Although not currently favoured experimentally this is still an interesting example for two reasons. Firstly the large width, compared to the case of a light Higgs just discussed, illustrates the behaviour of the MEM in the presence of a broad resonance. Secondly, although the current limits rule out a SM Higgs at approximately the  $2\sigma$  level, they do not rule out the possibility that some other (weaker) broad resonance could be found in the four lepton channel. Since in this example the Higgs boson has a large width we expect that the likelihood results will be different to the light Higgs example discussed previously.

We use the same background sample as in the previous examples and introduce four Higgs signal events that have been generated from an unweighted NLO sample. The results of a MEM likelihood analysis are presented in Fig. 8. We fit a parabola in the region  $410 \text{ GeV} < m_H < 450 \text{ GeV}$  in order to extract a best fit mass. We observe that in a similar fashion to the mass measurement examples that we have already presented, LO and NLO analyses return similar best fit masses and uncertainties:

$$m_H^{\text{fit}}(\text{LO}) = 428 \pm 14 \text{ GeV} , \quad m_H^{\text{fit}}(\text{NLO}) = 427 \pm 14 \text{ GeV} . \quad (5.4)$$

However, since the NLO model fits the data better than the LO model the NLO result is more significant compared to the background-only hypothesis.

A full understanding of the potential of the MEM for measuring heavy resonances that decay into leptons requires a detailed study involving many pseudo-experiments. Indeed since the width is so large one may often encounter individual experiments that include a small number of events with very large invariant mass. We expect this will result in a large spread of possible errors in the mass measurements. One can only perform a true comparison of the discriminating power of LO and NLO MEM analyses by investigating results obtained using an ensemble of pseudo-experiments. It is precisely this issue that we will investigate in more detail in the next section.

#### 5.5 A study with multiple pseudo experiments

In order to investigate the differences between the MEM at LO and NLO in a more systematic manner we repeat our analysis with multiple pseudo-experiments. We generate background-only data samples and study Higgs exclusion for a given Higgs mass hypothesis. We choose to investigate the case  $m_H = 200$  GeV since at this value the Higgs cross section is near its maximum in the four lepton channel. This means that, even with a smaller data set than in the previous examples, we can extract useful information from an individual pseudo-experiment.

Our setup is as follows. We generate 960 pseudo-experiments corresponding to unweighted NLO events using the tools described in the previous sections. We attempt to

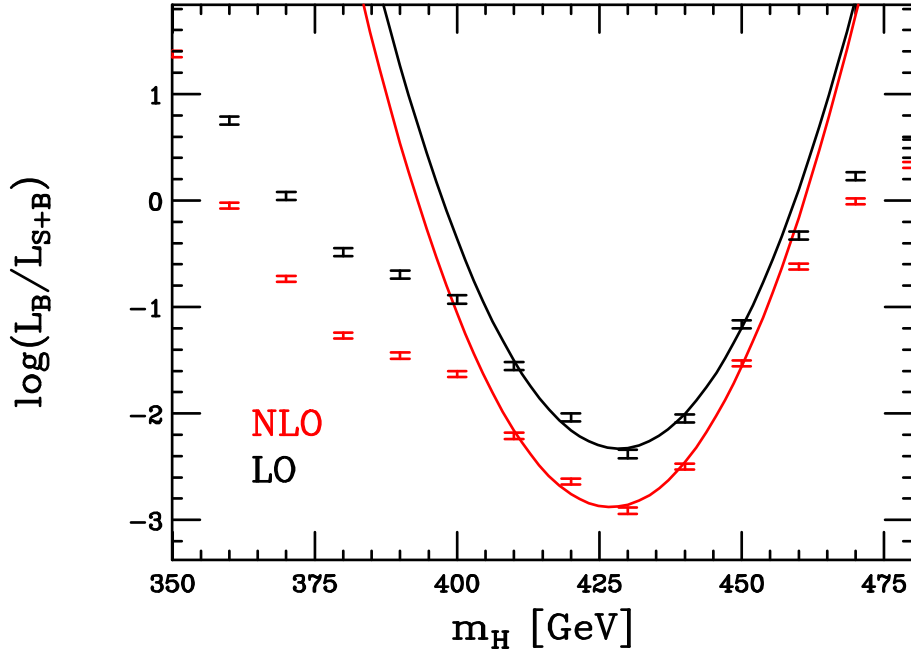


**Figure 8:** Log likelihoods for a heavy Higgs boson decaying into four leptons, where we have injected a signal at  $m_H = 425$  GeV.

generate the same number of background-only four lepton events as observed in the  $5 \text{ fb}^{-1}$  data set of each LHC experiment. This corresponds to approximately 70 events. Any given pseudo-experiment will contain a random fluctuation around this central value as a result of the unweighting procedure. When we generate our background-only samples each pseudo-experiment has equal weight, regardless of the number of events entering the sample. Clearly a pseudo-experiment with more events will be able to set better limits and we have not specifically accounted for this effect. However, since we are mostly interested in comparing the limits obtained at LO and NLO, this caveat should not greatly affect our conclusions.

In Fig. 9 we show the distribution of  $\Lambda = \log(L_B/L_{S+B})$  for the ensemble of pseudo-experiments. Since the signal at 200 GeV is relatively strong, a typical pseudo-experiment – that contains only background events – is able to exclude this hypothesis effectively, i.e.  $\Lambda > 0$ . We note that, as expected, the NLO MEM typically sets a much stronger exclusion than at LO (the peak in the LO distribution is in the region  $\Lambda \sim 5$ , whilst the NLO peak is at  $\Lambda \sim 9$ ). This is also clear from the summary of exclusion limits that could be set, presented in Table. 1.

Although it is interesting to examine the differences between the two orders in perturbation theory, we stress that it is not surprising that NLO is able to set stronger limits, since the event samples in each pseudo-experiment are generated by a NLO calculation. One might expect that if we had used LO unweighted samples instead, that LO would have set stronger limits for this Higgs mass. However, since NLO predictions typically provide a better description of experimental data than LO ones, there is some justification to the



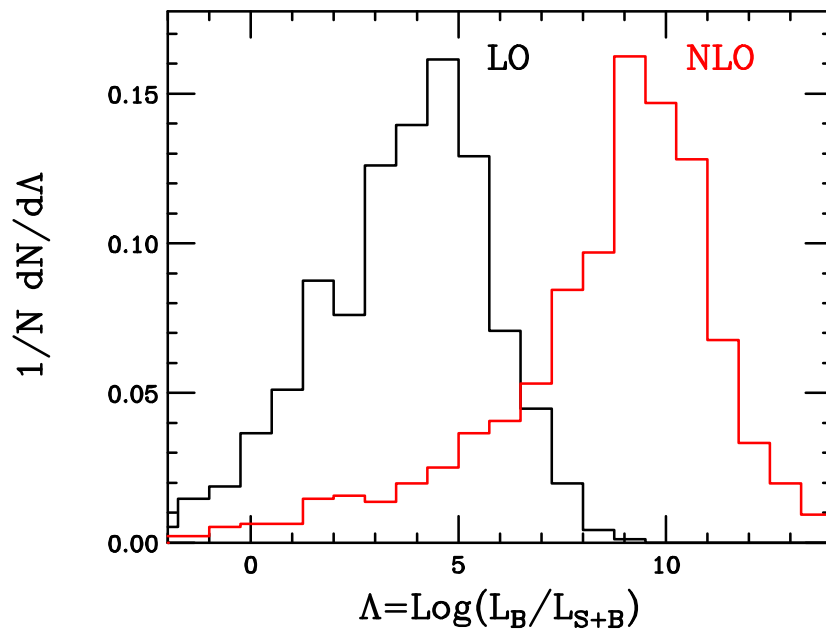


**Figure 9:** Pseudo experiments testing the hypothesis that there is a Higgs boson with  $m_H = 200$  GeV. We generate pseudo-experiments which consist only of background and no Higgs signal. As such the most common outcome is that the signal plus background hypothesis is less likely than the background only.

Exclusion	% LO	% NLO
$> 1\sigma$	91.1	98.2
$> 2\sigma$	77.3	96.1
$> 3\sigma$	38.1	90.1
$> 4\sigma$	0.521	67.3
$> 5\sigma$	0.00	3.75

**Table 1:** Percentage of pseudo experiments which set limits given by an upper bound on the confidence level.

claim that the NLO MEM could set stronger limits in such a Higgs search. In addition it is interesting to note that the likelihoods obtained at the two orders in perturbation theory are significantly different, regardless of which analysis sets the better limit. Given the large  $K$ -factors associated with these processes, this is not unexpected.

## 6. Conclusions

The matrix element method is an analysis technique that can be used to determine parameters of an underlying physics model by using a set of events that are measured experimentally. The probability that a single event in the set is described by a given model hypothesis can be computed from a calculation of the scattering probability within that model. Up

until now, the use of this technique had been limited to scattering probabilities computed at the leading order in perturbation theory, corresponding to Born matrix elements.

Even at leading order, a key issue that must be addressed is the means by which a generic experimental event is mapped to a scattering probability. In particular, such events typically contain additional hadronic activity that cannot be modelled by the simplest Born matrix elements. In this paper we have introduced a procedure for handling this mapping in a consistent manner. One can combine all of the event that is not part of the desired Born final state into one four vector,  $X$  and then boost into a frame in which  $X$  is at rest in the transverse plane. This feature does not uniquely define the boost and, although the matrix element is a Lorentz scalar, the convolution with the parton distribution functions depends on the specific nature of the boost. Therefore a theoretically well-defined procedure is only obtained by integrating over all allowed boosts. Once this has been done we can produce a well defined LO weight that can be associated with each experimental event.

We have subsequently illustrated how one can extend this method to next-to-leading order. The incorporation of some elements of the calculation, such as the virtual diagrams, is relatively straightforward since the diagrams share the same phase space as the Born calculation. The inclusion of the real radiation contribution is more complex and is performed by using a forward branching phase space generator. This allows one to maintain the exact kinematics of the Born event whilst integrating out the real radiation. We have used a slightly modified version of the usual Catani-Seymour dipole subtraction procedure in order to ensure event-by-event subtraction scheme independence. Using this generator we are able to define a map between all NLO events and Born phase space points. The final result is a method for generating a full NLO weight from a given Born phase space point. We note that there are some subtleties in this method that require particular care. For example, the difference between the lab- and MEM-frame transverse momentum can mean that events that are within the fiducial region in the lab frame cannot ultimately be included in a LO MEM analysis. At NLO, such events can be accommodated in a NLO MEM approach since they are accounted for by the presence of real radiation.

We have tested the method by producing NLO likelihoods for events that contain electroweak final states. As a first example we considered production of lepton pairs and showed that one could correctly measure the mass of the  $Z$  boson using events generated with Pythia. In this instance we observed that the MEM frame kinematics are very similar at LO and NLO. For this reason we only observed small differences between the MEM at LO and NLO for this process. We then considered the search for the Higgs boson in the channel  $gg \rightarrow H \rightarrow ZZ^* \rightarrow 4 \text{ leptons}$ . We showed that in this case the differences between the LO and NLO MEM analyses could be large. By using the NLO procedure one could obtain better limits on Higgs exclusion and observe stronger signals should a Higgs boson exist. In this case our input data was generated by a NLO parton level calculation, so it is perhaps not surprising that the NLO MEM analysis performed better than the LO one. Statements regarding possible improvements in results from the MEM at NLO are therefore predicated on the assumption that, in general, NLO predictions describe experimental data better than LO ones.

Future applications of the NLO MEM are widespread. One obvious example is the

measurement of the top quark mass. In addition the MEM is very useful when data samples are limited by statistics. Examples of measurements that would fall into this category include the measurement of the properties of the Higgs boson and limits on anomalous gauge boson couplings. We hope to extend our method to include more complicated final states, such as ones containing neutrinos and jets, shortly. The examples presented here have been implemented in a Fortran code that may be obtained from the authors on request.<sup>2</sup>

## Acknowledgments

We thank Oleg Brandt, Keith Ellis, Konstantin Matchev, Olivier Mattelaer and Gerben Stavenga for useful discussions. We thank Adam Martin for help with the Pythia sample generation. Fermilab is operated by Fermi Research Alliance, LLC under Contract No. DE-AC02-07CH11359 with the United States Department of Energy.

## A. An Initial State Forward Branching Phase Space Generator

In this appendix we will discuss the generation of the forward branching phase space (FBPS) used in our method, additional details for which can be found in refs. [38, 44]. To start the derivation of the initial state FBPS generator we recall the phase space for the production of a heavy state  $Q$  from two initial partons,  $\hat{p}_a$  and  $\hat{p}_b$ , as,

$$\frac{1}{2\hat{s}_{ab}} d\Phi_1^{[D]}(\hat{p}_a + \hat{p}_b \rightarrow Q) = \frac{2\pi}{2\hat{s}_{ab}} \delta(\hat{s}_{ab} - Q^2) . \quad (\text{A.1})$$

Here we have maintained the notation used in sec. 3, where hatted momenta indicate the underlying Born topology and unhatted momenta represent the phase space with one additional parton. The  $D$ -dimensional phase space for the emission of one extra initial state parton with momentum  $p_r$  is given by [44],

$$\begin{aligned} \frac{1}{2s_{ab}} d\Phi_1^{[D]}(p_a + p_b \rightarrow Q + p_r) &= \frac{(2\pi)^{1-D}}{4} \left( \frac{\hat{s}_{ab}}{s_{ab}^2} \right) \left( \frac{t_{ar} t_{rb}}{s_{ab}} \right)^{(D-4)/2} d t_{ar} d t_{rb} d\Omega^{[D-3]} \\ &\times \left[ \frac{2\pi}{2\hat{s}_{ab}} d\Phi_1^{[D]}(\hat{p}_a + \hat{p}_b \rightarrow Q) \right] \\ &= \frac{1}{2s_{ab}} d\Phi_{\text{FBPS}}^{[D]} \times \left[ \frac{2\pi}{2\hat{s}_{ab}} d\Phi_1^{[D]}(\hat{p}_a + \hat{p}_b \rightarrow Q) \right] . \end{aligned} \quad (\text{A.2})$$

We need the FBPS generator in four-dimensions,

$$d\Phi_{\text{FBPS}}^{[4]} = d\Phi_{\text{FBPS}} = \frac{1}{(2\pi)^3} \left( \frac{\hat{s}_{ab}}{s_{ab}} \right) d t_{ar} d t_{rb} d\phi , \quad (\text{A.3})$$

where  $\phi$  is the azimuthal angle around the  $z$ -axis,  $s_{xy}$  and  $t_{xy}$  are invariants defined through,  $s_{xy} = (p_x + p_y)^2$  and  $t_{xy} = (p_x - p_y)^2$ . While the above formula gives the phase space integrator, we need to derive both the integration boundaries and the explicit construction

---

<sup>2</sup>Please contact [ciaran@fnal.gov](mailto:ciaran@fnal.gov) for a copy of the code.

of the generated four-vectors ( $p_a$ ,  $p_b$  and  $p_r$ ) that are used in a numerical Monte Carlo integrator. The phase space generator starts using the input momenta  $\hat{p}_a$  and  $\hat{p}_b$ ,

$$\hat{p}_a = \hat{E}_a (1, 0, 0, -1) , \quad \hat{p}_b = \hat{E}_b (1, 0, 0, 1) , \quad (\text{A.4})$$

with  $\hat{s}_{ab} = 2\hat{p}_a \cdot \hat{p}_b = 4\hat{E}_a \hat{E}_b$ . We can eliminate  $t_{ar}$  in favour of  $s_{ab}$  by inserting the operator  $\int ds_{ab} \delta(s_{ab} + t_{ar} + t_{rb} - \hat{s}_{ab}) = 1$  to perform the  $t_{ar}$  integration,

$$d\Phi_{\text{FBPS}} = \left( \frac{\hat{s}_{ab}}{(2\pi)^3} \right) \int_{-t_{\min}}^0 dt_{rb} \int_{\hat{s}_{ab}}^s \left( \frac{ds_{ab}}{s_{ab}} \right) \int_0^{2\pi} d\phi . \quad (\text{A.5})$$

The integration limits on  $s_{ab}$  can be understood from the momentum conserving delta function and the requirement that  $t_{ar}, t_{rb} < 0$ . We will define  $t_{\min}$  shortly. Our task is then to construct the new momenta  $p_a$ ,  $p_b$  and  $p_r$  from the MC integration variables and determine the integration boundary  $t_{\min}$ . We relate  $s_{ab}$  and  $t_{rb}$  to our MC integration variable using logarithmic sampling,

$$\int_{\hat{s}_{ab}}^s \frac{ds_{ab}}{s_{ab}} = \log \left( \frac{s}{\hat{s}_{ab}} \right) \int_0^1 dr; \quad s_{ab}(r) = \hat{s}_{ab}^r s^{1-r} \quad (\text{A.6})$$

$$\begin{aligned} \int_{-t_{\min}}^0 dt_{br} &= \int_{-t_{\min}}^{-t_{\text{soft}}} dt_{br} + \int_{-t_{\text{soft}}}^0 dt_{br} \\ \int_{-t_{\min}}^{-t_{\text{soft}}} dt_{br} &= \log \left( \frac{t_{\min}}{t_{\text{soft}}} \right) \int_0^1 dr \, t_{rb}(r); \quad t_{rb}(r) = -(t_{\min})^r (t_{\text{soft}})^{1-r} . \end{aligned} \quad (\text{A.7})$$

Our phase space measure is now written in terms of MC integration variables and our final task is to determine  $p_a$ ,  $p_b$  and  $p_r$  for use in the matrix element in terms of our new variables. We wish to branch one of our initial state momenta and in this example we choose to branch  $\hat{p}_b$ . In order to do so we have to give it a virtuality  $t_{rb}$ , which we can do by boosting  $\hat{p}_a$ ,

$$\tilde{p}_a = (1 + \beta) \hat{p}_a , \quad \tilde{p}_b = \hat{p}_b - \beta \hat{p}_a , \quad (\text{A.8})$$

with  $\beta = -t_{rb}/\hat{s}_{ab}$ . Note that  $\hat{p}_a + \hat{p}_b = \tilde{p}_a + \tilde{p}_b = p_a - p_r + p_b$ . This means we have added to the phase space generator a factor  $\int d\beta \delta(\beta + t_{rb}/\hat{s}_{ab})$  that does not change the phase space weight. We define  $p_a = \tilde{p}_a = (1 + \beta) \hat{p}_a$  and parametrize  $p_b$  as follows,

$$p_b = z \hat{E}_b (1, \cos \theta, \sin \theta \cos \phi, \sin \theta \sin \phi) , \quad (\text{A.9})$$

where  $\theta$  is the polar angle with respect to momentum  $\hat{p}_b$ . Momentum conservation now fixes  $p_r = p_b - \tilde{p}_b = p_b - \hat{p}_b + \beta \hat{p}_a$ . To express  $\cos \theta$  and  $z$  in terms of the integration variables and the input energies we calculate the invariants

$$\begin{aligned} &\begin{cases} t_{ar} = (p_a - p_r)^2 = (\hat{p}_a + \hat{p}_b - p_b)^2 \\ t_{rb} = -2 p_r \cdot p_b = 2 \hat{p}_b \cdot p_b - 2 \beta \hat{p}_a \cdot p_b = 2 \hat{p}_b \cdot p_b + 2 (t_{rb}/\hat{s}_{ab}) \hat{p}_a \cdot p_b \end{cases} \quad (\text{A.10}) \\ \Rightarrow &\begin{cases} t_{ar} = 2 (\hat{p}_a \cdot \hat{p}_b - \hat{p}_a \cdot p_b - \hat{p}_b \cdot p_b) \\ t_{rb} = 2 (\hat{p}_a \cdot \hat{p}_b) (\hat{p}_b \cdot p_b) / (\hat{p}_a \cdot \hat{p}_b - \hat{p}_a \cdot p_b) \end{cases} \\ \Rightarrow &\begin{cases} t_{ar} = 4 \hat{E}_a \hat{E}_b - 2 z \hat{E}_b (\hat{E}_a + \hat{E}_b + (\hat{E}_a - \hat{E}_b) \cos \theta) \\ t_{rb} = 4 z \hat{E}_b^2 (1 - \cos \theta) / (2 - z(1 + \cos \theta)) \end{cases} . \end{aligned}$$

We can invert the equations to obtain.

$$\begin{aligned} z &= \frac{4\hat{E}_b^2(\hat{s}_{ab} - t_{ar} - t_{rb}) + t_{ar}t_{rb}}{4\hat{E}_b^2(\hat{s}_{ab} - t_{rb})} = \frac{4\hat{E}_b^2 s_{ab} + t_{ar}t_{rb}}{4\hat{E}_b^2(\hat{s}_{ab} - t_{rb})} \\ \cos\theta &= \frac{4\hat{E}_b^2(\hat{s}_{ab} - t_{ar} - t_{rb}) - t_{ar}t_{rb}}{4\hat{E}_b^2(\hat{s}_{ab} - t_{ar} - t_{rb}) + t_{ar}t_{rb}} = \frac{4\hat{E}_b^2 s_{ab} - t_{ar}t_{rb}}{4\hat{E}_b^2 s_{ab} + t_{ar}t_{rb}}. \end{aligned} \quad (\text{A.11})$$

By choosing

$$t_{\min} = \min(s_{ab} - \hat{s}_{ab}, \hat{s}_{ab}(\sqrt{s} - \hat{E}_a)/\hat{E}_a),$$

we fulfill the requirement  $-1 < \cos\theta < 1$ . Remaining constraints (such as a jet-veto on  $p_r$ ) are imposed through event vetos.

We have thus illustrated how we have implemented the FBPS to perform both the integration over emitted partons and the phase space generation of  $p_a$ ,  $p_b$  and  $p_r$  for use in the matrix element. The input for the generator is just the Born kinematics, i.e.  $\hat{p}_a$ ,  $\hat{p}_b$  and  $Q$ .

## B. Subtraction terms in the MEM frame

In this appendix we discuss the modifications to the Catani-Seymour dipoles [37] needed to correctly ensure a one-to-one map between the integrated and unintegrated subtractions on an event by event basis. In this paper we consider processes with electroweak final states, and as such only need initial-initial dipoles. In the standard approach one would perform a transformation such that the emitter and spectator are kept along the beam axis, with a Lorentz transformation on the remaining final state particles performed in order to ensure momentum conservation. In our case it is essential to keep the final state particles fixed and instead change the momenta of the initial state partons.

The standard Catani Seymour dipole keeps the momentum of the spectator initial particle  $b$  fixed, while the emitter  $a$  is rescaled by an amount  $x_{a,r}$ ,

$$\begin{aligned} \tilde{p}_{ar} &= x_{a,r} p_a, \\ x_{r,ab} &= \frac{s_{ab} + s_{ar} + s_{rb}}{s_{ab}}. \end{aligned} \quad (\text{B.1})$$

Here we have kept the same notation as the previous section, with  $r$ ,  $a$  and  $b$  representing the emitted parton, initial state emitter and initial state spectator respectively. Hatted momenta still represent the underlying Born phase space – with unhatted momenta indicating the real phase space point – and in addition  $\tilde{p}$  now represents the dipole phase space point. The transformation above is given by Eqs. (5.137) and (5.138) in Ref. [37] using our momentum definitions. In order to ensure that  $\tilde{p}$  is a correct phase space point one must perform a Lorentz transformation (Eqs. (5.139) - (5.144) in Ref. [37]) to ensure momentum conservation.

The above transformation is not ideal for our setup. This is because the Lorentz transformation will naturally change the underlying Born phase space point. This means that there will not be a one-to-one correspondence between real and virtual events and only

the sum over all virtual and real contributions will be well-defined. In order to maintain our exact map to the Born phase space  $\hat{p}_a + \hat{p}_b \rightarrow Q$  we replace Eq. (B.1) by the following transformation,

$$\tilde{p}_{ar} = x_{a,r} \hat{p}_a , \quad (\text{B.2})$$

$$x_{r,ab} = \frac{s_{ab} + s_{ar} + s_{rb}}{s_{ab}} . \quad (\text{B.3})$$

Note that the transformation acts on  $\hat{p}_a$ , the initial state momentum of the Born phase space. We note that this transformation preserves momentum conservation in the transverse plane, but not in the longitudinal plane. Therefore the correct dipole phase space point is at a different  $x_a$  and  $x_b$  than the original Born phase space point. Since we integrate over these variables this is sufficient to obtain the exact mapping between virtual and real contributions on an event by event basis. Using our new transformation we can implement the usual Catani-Seymour dipole formulae (Eqs. (5.145) - (5.156) in Ref. [37]).

## References

- [1] **ATLAS Collaboration** Collaboration, G. Aad *et. al.*, *Combined search for the Standard Model Higgs boson using up to 4.9 fb-1 of pp collision data at sqrt(s) = 7 TeV with the ATLAS detector at the LHC*, *Phys.Lett.* **B710** (2012) 49–66, [[arXiv:1202.1408](#)].
- [2] **CMS Collaboration** Collaboration, S. Chatrchyan *et. al.*, *Combined results of searches for the standard model Higgs boson in pp collisions at sqrt(s) = 7 TeV*, [arXiv:1202.1488](#).
- [3] **ATLAS Collaboration** Collaboration, G. Aad *et. al.*, *Search for the Standard Model Higgs boson in the diphoton decay channel with 4.9 fb-1 of pp collisions at sqrt(s)=7 TeV with ATLAS*, *Phys.Rev.Lett.* **108** (2012) 111803, [[arXiv:1202.1414](#)].
- [4] **CMS Collaboration** Collaboration, S. Chatrchyan *et. al.*, *Search for the standard model Higgs boson decaying into two photons in pp collisions at sqrt(s)=7 TeV*, [arXiv:1202.1487](#).
- [5] Y. Gao, A. V. Gritsan, Z. Guo, K. Melnikov, M. Schulze, *et. al.*, *Spin determination of single-produced resonances at hadron colliders*, *Phys.Rev.* **D81** (2010) 075022, [[arXiv:1001.3396](#)].
- [6] A. De Rujula, J. Lykken, M. Pierini, C. Rogan, and M. Spiropulu, *Higgs look-alikes at the LHC*, *Phys.Rev.* **D82** (2010) 013003, [[arXiv:1001.5300](#)].
- [7] **CDF Collaboration**, T. Aaltonen *et. al.*, *Evidence for a Mass Dependent Forward-Backward Asymmetry in Top Quark Pair Production*, *Phys. Rev.* **D83** (2011) 112003, [[arXiv:1101.0034](#)].

- [8] **D0 Collaboration** Collaboration, V. M. Abazov *et. al.*, *Forward-backward asymmetry in top quark-antiquark production*, *Phys.Rev.* **D84** (2011) 112005, [[arXiv:1107.4995](#)].
- [9] K. Kondo, *Dynamical likelihood method for reconstruction of events with missing momentum. 2: Mass spectra for  $2 \rightarrow ; 2$  processes*, *J.Phys.Soc.Jap.* **60** (1991) 836–844.
- [10] R. Dalitz and G. R. Goldstein, *The Decay and polarization properties of the top quark*, *Phys.Rev.* **D45** (1992) 1531–1543.
- [11] **D0 Collaboration** Collaboration, V. Abazov *et. al.*, *A precision measurement of the mass of the top quark*, *Nature* **429** (2004) 638–642, [[hep-ex/0406031](#)].
- [12] **D0 Collaboration** Collaboration, V. Abazov *et. al.*, *Measurement of the top quark mass in the lepton+jets final state with the matrix element method*, *Phys.Rev.* **D74** (2006) 092005, [[hep-ex/0609053](#)].
- [13] **CDF Collaboration** Collaboration, A. Abulencia *et. al.*, *Precise measurement of the top quark mass in the lepton+jets topology at CDF II*, *Phys.Rev.Lett.* **99** (2007) 182002, [[hep-ex/0703045](#)].
- [14] **CDF - Run II Collaboration** Collaboration, A. Abulencia *et. al.*, *Precision measurement of the top quark mass from dilepton events at CDF II*, *Phys.Rev.* **D75** (2007) 031105, [[hep-ex/0612060](#)].
- [15] **D0 Collaboration** Collaboration, V. Abazov *et. al.*, *Measurement of the top quark mass in the dilepton channel*, *Phys.Lett.* **B655** (2007) 7–14, [[hep-ex/0609056](#)].
- [16] F. Fiedler, A. Grohsjean, P. Haefner, and P. Schieferdecker, *The Matrix Element Method and its Application in Measurements of the Top Quark Mass*, *Nucl.Instrum.Meth.* **A624** (2010) 203–218, [[arXiv:1003.1316](#)].
- [17] **D0 Collaboration** Collaboration, V. Abazov *et. al.*, *Evidence for production of single top quarks*, *Phys.Rev.* **D78** (2008) 012005, [[arXiv:0803.0739](#)].
- [18] **CDF Collaboration** Collaboration, T. Aaltonen *et. al.*, *Observation of Single Top Quark Production and Measurement of  $\sigma(Vtb)$  with CDF*, *Phys.Rev.* **D82** (2010) 112005, [[arXiv:1004.1181](#)]. Submitted to Phys. Rev. D.
- [19] **CDF Collaboration** Collaboration, T. Aaltonen *et. al.*, *First Observation of Electroweak Single Top Quark Production*, *Phys.Rev.Lett.* **103** (2009) 092002, [[arXiv:0903.0885](#)].
- [20] **D0 Collaboration** Collaboration, V. Abazov *et. al.*, *Observation of Single Top Quark Production*, *Phys.Rev.Lett.* **103** (2009) 092001, [[arXiv:0903.0850](#)].
- [21] **D0 Collaboration**, V. M. Abazov *et. al.*, *Evidence for spin correlation in  $t\bar{t}$  production*, [arXiv:1110.4194](#).

- [22] **CDF Collaboration** Collaboration, T. Aaltonen *et. al.*, *Search for Standard Model Higgs Boson Production in Association with a W Boson Using a Matrix Element Technique at CDF in  $p\bar{p}$  Collisions at  $\sqrt{s} = 1.96$  TeV*, [arXiv:1112.4358](#).
- [23] **CMS Collaboration**, S. Chatrchyan *et. al.*, *Measurement of the weak mixing angle with the Drell-Yan process in proton-proton collisions at the LHC*, [arXiv:1110.2682](#).
- [24] J. Alwall, M. Herquet, F. Maltoni, O. Mattelaer, and T. Stelzer, *MadGraph 5 : Going Beyond*, *JHEP* **1106** (2011) 128, [[arXiv:1106.0522](#)].
- [25] T. Gleisberg and S. Hoeche, *Comix, a new matrix element generator*, *JHEP* **0812** (2008) 039, [[arXiv:0808.3674](#)].
- [26] W. Kilian, T. Ohl, and J. Reuter, *WHIZARD: Simulating Multi-Particle Processes at LHC and ILC*, *Eur.Phys.J.* **C71** (2011) 1742, [[arXiv:0708.4233](#)].
- [27] **CompHEP Collaboration** Collaboration, E. Boos *et. al.*, *CompHEP 4.4: Automatic computations from Lagrangians to events*, *Nucl.Instrum.Meth.* **A534** (2004) 250–259, [[hep-ph/0403113](#)].
- [28] M. L. Mangano, M. Moretti, F. Piccinini, R. Pittau, and A. D. Polosa, *ALPGEN, a generator for hard multiparton processes in hadronic collisions*, *JHEP* **0307** (2003) 001, [[hep-ph/0206293](#)].
- [29] P. Artoisenet, V. Lemaître, F. Maltoni, and O. Mattelaer, *Automation of the matrix element reweighting method*, *JHEP* **1012** (2010) 068, [[arXiv:1007.3300](#)].
- [30] J. M. Campbell and R. K. Ellis, *An update on vector boson pair production at hadron colliders*, *Phys. Rev.* **D60** (1999) 113006, [[hep-ph/9905386](#)].
- [31] J. M. Campbell and R. K. Ellis, *MCFM for the Tevatron and the LHC*, *Nucl.Phys.Proc.Suppl.* **205-206** (2010) 10–15, [[arXiv:1007.3492](#)]. Talk presented by R.K Ellis at Loops and Legs in Quantum Field Theory 2010, Woerlitz, Germany, April 25-30, 2010.
- [32] J. M. Campbell, R. K. Ellis, and C. Williams, *Vector boson pair production at the LHC*, *JHEP* **07** (2011) 018, [[arXiv:1105.0020](#)].
- [33] MCFM web page, <http://mcfm.fnal.gov/>, .
- [34] T. Sjostrand, S. Mrenna, and P. Z. Skands, *A Brief Introduction to PYTHIA 8.1*, *Comput.Phys.Comm.* **178** (2008) 852–867, [[arXiv:0710.3820](#)].
- [35] G. Cowan, *Statistical Data Analysis*, Oxford Science Publications (1998).
- [36] J. Alwall, A. Freitas, and O. Mattelaer, *The Matrix Element Method and QCD Radiation*, *Phys. Rev.* **D83** (2011) 074010, [[arXiv:1010.2263](#)].



- [37] S. Catani and M. Seymour, *A General algorithm for calculating jet cross-sections in NLO QCD*, *Nucl.Phys.* **B485** (1997) 291–419, [[hep-ph/9605323](#)].
- [38] W. T. Giele, G. C. Stavenga, and J.-C. Winter, *A Forward Branching Phase-Space Generator*, [arXiv:1106.5045](#).
- [39] **ATLAS Collaboration** Collaboration, G. Aad *et. al.*, *Search for the Standard Model Higgs boson in the decay channel  $H \rightarrow ZZ(^*) \rightarrow 4l$  with 4.8 fb<sup>-1</sup> of pp collision data at  $\sqrt{s} = 7$  TeV with ATLAS*, *Phys. Lett.* **B710** (2012) 383–402, [[arXiv:1202.1415](#)].
- [40] **CMS Collaboration** Collaboration, S. Chatrchyan *et. al.*, *Search for the standard model Higgs boson in the decay channel  $H$  to  $ZZ$  to 4 leptons in pp collisions at  $\sqrt{s} = 7$  TeV*, [arXiv:1202.1997](#).
- [41] J. S. Gainer, K. Kumar, I. Low, and R. Vega-Morales, *Improving the sensitivity of Higgs boson searches in the golden channel*, [arXiv:1108.2274](#).
- [42] A. D. Martin, W. J. Stirling, R. S. Thorne, and G. Watt, *Parton distributions for the LHC*, *Eur. Phys. J.* **C63** (2009) 189–285, [[arXiv:0901.0002](#)].
- [43] J. M. Campbell, R. K. Ellis, and C. Williams, *Gluon-gluon contributions to  $W^+ W^-$  production and Higgs interference effects*, *JHEP* **10** (2011) 005, [[arXiv:1107.5569](#)].
- [44] W. Giele, E. Glover, and D. A. Kosower, *Higher order corrections to jet cross-sections in hadron colliders*, *Nucl.Phys.* **B403** (1993) 633–670, [[hep-ph/9302225](#)].